White Rose Research Online

eprints@whiterose.ac.uk
https://eprints.whiterose.ac.uk
Universities of Leeds, Sheffield and York

Deposited via The University of Leeds.

White Rose Research Online URL for this paper:
https://eprints.whiterose.ac.uk/id/eprint/172082/

Version: Accepted Version

Article:
Kunitomo, M, Ida, S, Takeuchi, T et al. (2021) Photoevaporative Dispersal of Protoplanetary Disks around Evolving Intermediate-mass Stars. The Astrophysical Journal, 909 (2). 109. ISSN: 0004-637X

https://doi.org/10.3847/1538-4357/abdb2a

© 2021. The American Astronomical Society. This is an author produced version of a journal article published in The Astrophysical Journal. Uploaded in accordance with the publisher's self-archiving policy.

Reuse
Items deposited in White Rose Research Online are protected by copyright, with all rights reserved unless indicated otherwise. They may be downloaded and/or printed for private study, or other acts as permitted by national copyright laws. The publisher or other rights holders may allow further reproduction and re-use of the full text version. This is indicated by the licence information on the White Rose Research Online record for the item.

Takedown
If you consider content in White Rose Research Online to be in breach of UK law, please notify us by emailing eprints@whiterose.ac.uk including the URL of the record and the reason for the withdrawal request.

UNIVERSITY OF LEEDS
University of Sheffield
UNIVERSITY of York

Draft version January 10, 2021
Typeset using LaTeX **twocolumn** style in AASTeX63

Photoevaporative dispersal of protoplanetary disks around evolving intermediate-mass stars

Masanobu Kunitomo [1], Shigeru Ida [2], Taku Takeuchi [3,*], Olja Panić [4,†], James M. Miley [4,5,6] and Takeru K. Suzuki [7]

[1] Department of Physics, School of Medicine, Kurume University, 67 Asahimachi, Kurume, Fukuoka 830-0011, Japan
[2] Earth-Life Science Institute, Tokyo Institute of Technology, 2-12-1 Ookayama, Meguro-ku, Tokyo 152-8551, Japan
[3] Department of Earth and Planetary Sciences, Tokyo Institute of Technology, 2-12-1 Ookayama, Meguro-ku, Tokyo 152-8551, Japan
[4] School of Physics and Astronomy, University of Leeds, Leeds LS2 9JT, UK
[5] Joint ALMA Observatory, Alonso de Cordova 3107, Vitacura, Santiago, Chile
[6] National Astronomical Observatory of Japan, Alonso de Cordova 3788, 61B Vitacura, Santiago, Chile
[7] School of Arts & Sciences, The University of Tokyo, 3-8-1, Komaba, Meguro, Tokyo 153-8902, Japan

(Received ***; Revised ***; Accepted **)

Submitted to ApJ

ABSTRACT

We aim to understand the effect of stellar evolution on the evolution of protoplanetary disks. We in particular focus on the disk evolution around intermediate-mass (IM) stars, which evolve more rapidly than low-mass ones. We numerically solve the long-term evolution of disks around 0.5–5 $M_\odot$ stars considering viscous accretion and photoevaporation (PE) driven by stellar far-ultraviolet (FUV), extreme-ultraviolet (EUV) and X-ray emission. We also take stellar evolution into account and consider the time evolution of the PE rate. We find that the FUV, EUV and X-ray luminosities of IM stars evolve by orders of magnitude within a few Myr along with the time evolution of stellar structure, stellar effective temperature or accretion rate. Therefore, the PE rate also evolves with time by orders of magnitude and we conclude that stellar evolution is crucial for the disk evolution around IM stars.

Keywords: accretion, accretion disks — planetary systems: protoplanetary disks — stars: winds, outflows — stars: evolution — stars: pre-main-sequence

1. INTRODUCTION

So far the long-term evolution of protoplanetary disks has been mostly investigated by considering the viscous accretion and photoevaporation (e.g., Clarke et al. 2001; Alexander et al. 2006a; Gorti et al. 2009; Owen et al. 2010). Photoevaporation (PE hereafter) is a thermally driven disk wind from hot disk atmospheres due to the irradiation of high-energy photons (e.g., Hollenbach et al. 1994), that is, far-ultraviolet photons (FUV; 6–13.6 eV), extreme-ultraviolet photons (EUV; 13.6–100 eV) and X-rays (> 100 eV). Most of the previous works, however, do not consider the time evolution of the luminosity of high-energy photons, and do not include all PE mechanisms.

Gorti et al. (2009) investigated the long-term disk evolution considering all PE mechanisms from central stars for the first time. However, they did not consider the temporal evolution of the luminosity of EUV and X-rays. Moreover, the contribution of each mechanism was not clearly shown. Since the PE rate depends on the UV and X-ray luminosities, it is crucial for disk evolutionary models to adopt realistic models of those luminosities. We also note that Alexander et al. (2004) claimed that FUV and EUV from the stellar photosphere are sensitive to the absorption in the stellar atmosphere.

In this paper we aim to (i) investigate the long-term disk evolution (i.e., not dynamical evolution within several Kepler timescales but the disk evolution for Myr) with realistic FUV, EUV, and X-ray luminosity, considering stellar evolution and the absorption in the stellar

Corresponding author: Masanobu Kunitomo
kunitomo.masanobu@gmail.com

* Present affiliation: Sanoh Industrial Co., Ltd., Japan
† Royal Society Dorothy Hodgkin Fellow

atmosphere, and (ii) clarify which mechanism of the PE plays a dominant role in dispersing disks.

We in particular focus on the influence of stellar evolution. As we will describe in detail in Sect. 2, young stars emit UV photons and X-rays through three mechanisms: magnetic activity, accretion shock, and photospheric radiation. Since the magnetic activity originates from the convective motion in the stellar interior, the evolution of stellar internal structure (i.e., the thickness of the convective envelope, $M_{\rm conv}$) is important (see Sect. 2.5). The $M_{\rm conv}$ value of young stars decreases with time and instead a radiative core is developed. Moreover, the spectra of photospheric radiation depends on the stellar effective temperature, $T_{\rm eff}$ (see Sect. 2.2). These quantities, $M_{\rm conv}$ and $T_{\rm eff}$, of young stars evolve on the Kelvin-Helmholtz (K-H) timescale,

$$\tau_{\rm KH} = c\frac{GM_\star^2}{R_\star L_\star} = 6.7\,{\rm Myr}\left(\frac{M_\star}{\rm M_\odot}\right)^2\left(\frac{R_\star}{2\,\rm R_\odot}\right)^{-1}\left(\frac{L_\star}{\rm L_\odot}\right)^{-1}\left(\frac{c}{3/7}\right) \quad (1)$$

where $M_\star$ is the stellar mass, $R_\star$ the stellar radius and $L_\star$ the stellar intrinsic bolometric luminosity, and c is a dimensionless factor which depends on the polytropic index (e.g., $c = 3/7$ for fully convective stars and 3/4 for radiative stars). Given the weak dependence of $L_\star$ of pre-main-sequence (pre-MS hereafter) stars on $M_\star$ (i.e., roughly $L_\star \propto M_\star^2$ for pre-MS stars), $\tau_{\rm KH}$ of higher-mass stars is shorter and thus $T_{\rm eff}$ and $M_{\rm conv}$ of higher-mass stars evolve more rapidly. Therefore, the PE rate is also expected to change with time, in particular around higher-mass stars.

We note that recent infrared (IR hereafter) observations have revealed that the disk evolution around intermediate-mass (IM hereafter) stars is different from low-mass stars in the following three respects: the near-IR dust disk lifetime of IM stars is shorter than low-mass stars (Hillenbrand et al. 1992; Hernández et al. 2005; Carpenter et al. 2006; Yasui et al. 2014; Ribas et al. 2015), the Hα gas disk lifetime is also shorter (Kennedy & Kenyon 2009; Yasui et al. 2014), and there is a substantial difference between near-IR and mid-IR dust disk lifetimes unlike low-mass stars (Yasui et al. 2014). Therefore disk evolution depends on stellar mass. Following previous studies above, we define IM as stars of mass above 2–5 $\rm M_\odot$[1]. There is also a difference in planetary architectures between low-mass and IM stars (i.e., lack of close-in planets around IM stars), which may result from the different disk evolution (e.g., Burkert & Ida 2007; Sato et al. 2008; Currie 2009; Kunitomo et al. 2011). For the understanding of these puzzles, as a first step we investigate the effect of stellar evolution on disk evolution in this paper.

This paper is organized as follows. First we describe our model of the luminosity of the high-energy photons considering stellar evolution. In Sect. 3, we describe our physical models of the PE and computation method for simulating the disk evolution. In Sect. 4, we investigate how the disk evolution is affected by stellar evolution. In Sect. 5, we describe the caveats of our model. The results are summarized in Sect. 6.

2. STELLAR EVOLUTION

In this section, first we describe the computation methods of the stellar evolution (Sect. 2.1) and the stellar atmosphere (Sect. 2.2). Using these results and the observational results, we model the evolution of stellar FUV, EUV and X-ray luminosity (Sects. 2.3–2.5).

2.1. *Stellar evolution calculation*

We simulate the stellar evolution using the code `MESA` (Paxton et al. 2011) (ver. 2258, see also Kunitomo et al. 2011, for the details). Figure 1 shows the evolutionary tracks of 0.5–5 $\rm M_\odot$ stars in the Hertzsprung-Russell (H-R) diagram. We assume the solar metallicity. We adopt the birthline of Stahler & Palla (2005) in the H-R diagram as an initial condition. This corresponds to the standard scenario of star formation (see Sect. 5.4). We note that the luminosity of 0.8–2 $\rm M_\odot$ stars on the birthline is almost the same because of the short thermal timescale, whereas that of $> 2\,\rm M_\odot$ stars increases with $M_\star$ because of deuterium burning (Stahler 1988).

Here we briefly introduce the basic nature of the stellar pre-MS evolution (see, e.g., Kippenhahn & Weigert 1990; Stahler & Palla 2005). From the birthline, young low-mass stars evolve along their Hayashi track, which is almost vertical in the H-R diagram due to the strong temperature dependence of the $\rm H^-$ opacity (Hayashi 1961). On the Hayashi track, stars are fully convective and shrink due to the radiative energy loss (i.e., the K-H contraction). Since the energy loss results in the increasing internal temperature with time from the virial theorem and the stellar internal opacity is anti-correlated with temperature (i.e., the Kramers law), the stellar internal opacity decreases with time. Then a radiative core is developed and a star leaves the Hayashi track. We note that high-mass ($> 3\,\rm M_\odot$) stars are hot enough to have a radiative core from the beginning. Stars evolve on the horizontal Henyey track and the stellar effective

[1] We note that Hernández et al. (2005) and Ribas et al. (2015) defined $> 2\,\rm M_\odot$ stars as Herbig Ae/Be and high-mass stars, respectively, whereas Yasui et al. (2014) defined 1.5–7 $\rm M_\odot$ stars as IM stars.

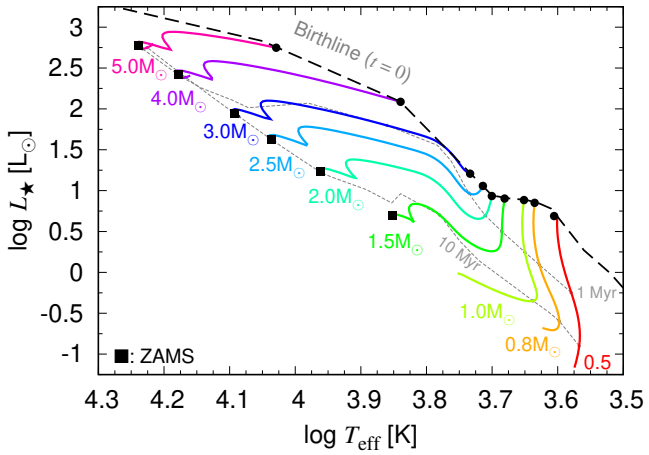

Figure 1. Evolutionary tracks of young, 0.5–5 $M_\odot$ stars (from right to left) from the birthline (the black dashed line, Stahler & Palla 2005) to 30 Myr in the H-R diagram. The squares represent the zero-age main sequence (ZAMS). The two gray dashed lines show the 1 Myr (top) and 10 Myr (bottom) isochrones.

temperature, $T_{\rm eff}$, increases with time. The IM pre-MS stars with a high $T_{\rm eff}$ surrounded by a disk are called Herbig Ae/Be stars (Herbig 1960; van den Ancker et al. 1997). The evolution of stellar structure and $T_{\rm eff}$ is a key ingredient in this work (see Sects. 2.2 and 2.5).

We do not consider for simplicity the $M_\star$ evolution due to the mass accretion from the disk inner edge to the star or the mass loss via stellar winds (e.g., Suzuki et al. 2013).

2.2. *Stellar spectra and atmospheric model*

UV photons are directly emitted from the photosphere of hot IM stars. Those photons, however, are substantially absorbed in the stellar atmosphere and therefore the stellar spectra deviate from the blackbody (Alexander et al. 2004). Here we quantify the extent of the absorption of UV photons by using a stellar atmospheric model. In this subsection we describe the method and results.

We used version 13.04 of the `Cloudy` code, last described by Ferland et al. (2013), to obtain spectra. We note that the stellar evolution simulations in `MESA` do not provide stellar spectra. Therefore we need to independently calculate the stellar absorption using the `Cloudy` code. We adopt the Atlas grids of Castelli & Kurucz (2003) **in the case of the solar metallicity**, which are available in $T_{\rm eff}$ = 3500–50000 K. We assume $R_\star = 1\,R_\odot$ and the Stefan-Boltzmann law gives the bolometric luminosity $L_\star$. We adopt the stellar surface gravity $g = 0.33\,g_\odot$, where $g_\odot = 10^{4.44}$ cm/s^2 is the surface gravity of the Sun. We note that the results below are not sensitive to the assumed g value (see Appendix A) nor $R_\star$.

Figure 2a shows the stellar spectra as a function of wavelength λ in the cases of $T_{\rm eff}$ = 20776, 15097, 10128, 7971 and 3587 K with and without the absorption in the stellar atmosphere. We note that the latter (i.e., the blackbody spectra) is $\pi\nu B_\nu$, where ν is the frequency and B_ν the Planck function. The spectra exhibit the strong absorption at the Lyman break and in the EUV range ($>$ 13.6 eV), and therefore we should not use the blackbody for $\Phi_{\rm EUV,ph}$ as claimed in Alexander et al. (2004). We also find the absorption in the FUV (not only the Lyman α absorption at 1216 Å) in the case with the low $T_{\rm eff}$. We note that we confirmed that the spectrum of a 15097 K star is almost the same as Fig. 1 of Alexander et al. (2004).

We define the fraction of the photospheric EUV luminosity $L_{\rm EUV,ph}$ to $L_\star$ as

$$f_{\rm EUV}(T_{\rm eff}) = L_{\rm EUV,ph}/L_\star\,. \tag{2}$$

We simply assume 50 eV as the average EUV photon energy and $\Phi_{\rm EUV,ph} = L_{\rm EUV,ph}/50\,{\rm eV}$. In practice, with the stellar spectra, we calculate $f_{\rm EUV}(T_{\rm eff})$ by $f_{\rm EUV} \equiv \int_{13.6\ {\rm eV}}^{100\ {\rm eV}} F_\nu d\nu/(\sigma_{\rm SB}T_{\rm eff}^4)$. We also define $f_{\rm FUV}(T_{\rm eff}) = L_{\rm FUV,ph}/L_\star$, where $L_{\rm FUV,ph}$ is the photospheric FUV luminosity.

Figure 2b shows the results of $f_{\rm EUV}$ and $f_{\rm FUV}$ as a function of $T_{\rm eff}$. Using the polynomial fitting of Numpy, we obtained the following fitting formulae:

$$\log f_{\rm EUV} = \sum_{i=0}^{5} a_i (\log T_{\rm eff})^i \tag{3}$$

in 5000–50000 K, where $a_5 = -95.238145$, $a_4 = 1998.2116$, $a_3 = -16728.880$, $a_2 = 69832.410$, $a_1 = -145282.56$, $a_0 = 120432.67$, and

$$\log f_{\rm FUV} = \sum_{i=0}^{6} b_i (\log T_{\rm eff})^i \tag{4}$$

in the range of $T_{\rm eff}$ = 3500–50000 K, where $b_6 = 177.14306$, $b_5 = -4452.9922$, $b_4 = 46546.370$, $b_3 = -258939.74$, $b_2 = 808484.59$, $b_1 = -1343172.0$, $b_0 = 927492.51$.

We set $f_{\rm EUV} = 0$ where $T_{\rm eff} < 5\times10^3$ K and $f_{\rm FUV} = 0$ where $< 3.5 \times 10^3$ K. Together with the evolution of $T_{\rm eff}$ and $L_\star$, we obtain the evolutions of $\Phi_{\rm EUV,ph}$ and $L_{\rm FUV,ph}$.

Figure 3 shows the results of the $L_{\rm FUV,ph}$ evolution of 1.5–5 $M_\odot$ stars and the $\Phi_{\rm EUV,ph}$ evolution of 3–5 $M_\odot$. We have combined $T_{\rm eff}(t)$ and $L_\star(t)$ from the stellar evolution simulations (see Sect. 2) and the $f_{\rm FUV}$ and $f_{\rm EUV}$

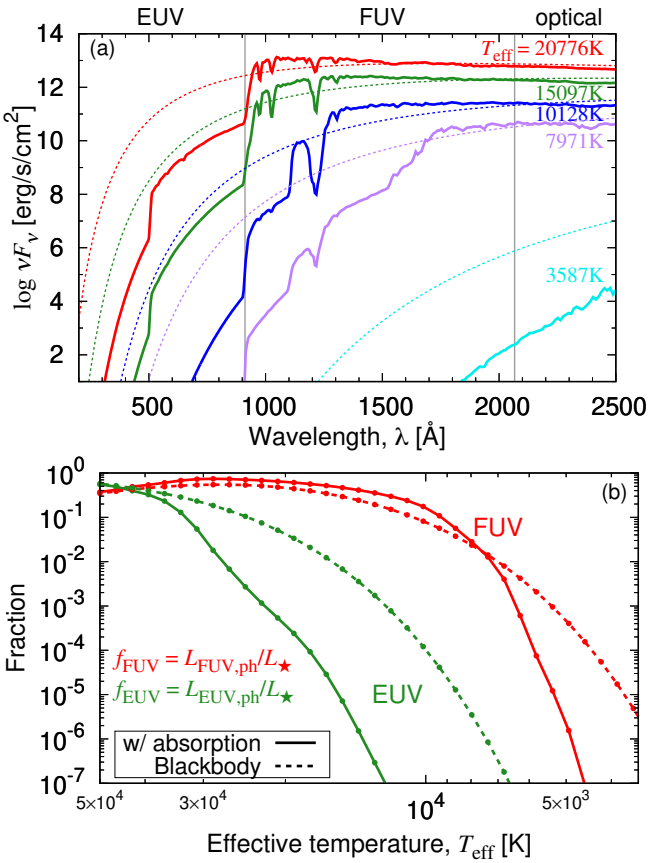

Figure 2. The solid and dotted lines show the results with and without the absorption in the stellar atmosphere (Castelli & Kurucz 2003), respectively (i.e., the latter is the blackbody spectra), in the case of $g = 0.33\,{\rm g}_\odot$. (Top panel) Stellar spectra in the cases of $T_{\rm eff}$ = 20776, 15097, 10128, 7971 and 3587 K from top to bottom. The two vertical lines indicate the wavelength at 6 and 13.6 eV. (Bottom) $f_{\rm FUV}$ (red) and $f_{\rm EUV}$ (green) (see text).

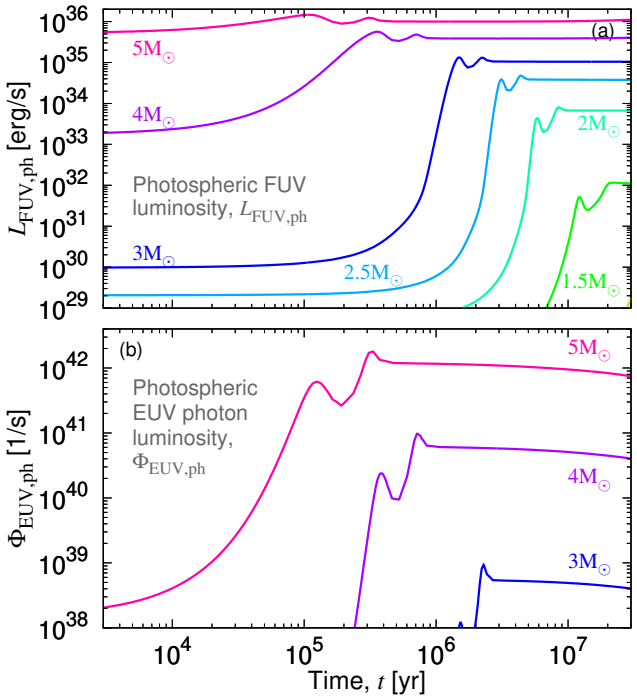

Figure 3. Time evolution of the photospheric FUV luminosity, $L_{\rm FUV,ph}$, of 1.5–5 $\rm M_\odot$ stars (top panel) and the photospheric EUV photon luminosity, $\Phi_{\rm EUV}$, of 3–5 $\rm M_\odot$ stars (bottom panel).

relations (see the solid lines in Fig. 2b). We find that they abruptly increase by orders of magnitude. Equation (4) shows that $T_{\rm eff} = 7342$ K is a characteristic temperature: above this temperature, $f_{\rm FUV}$ exceeds 10^{-2}. We will show the influence of this rapid increase on the disk evolution in Sect. 4.

Gorti et al. (2009) investigated disk evolution including $L_{\rm FUV,ph}$ and $\Phi_{\rm EUV,ph}$. They adopted those values of MS stars from Parravano et al. (2003): $L_{\rm FUV,ph} = 3.8\times10^{33}, 2.9\times10^{34}, 1.1\times10^{35}, 4.3\times10^{35}$ and 1.3×10^{36} erg/s for 2, 2.5, 3, 4 and 5 $\rm M_\odot$ stars, whereas $\Phi_{\rm EUV,ph} = 2.4\times10^{42}\,{\rm s}^{-1}$ for a 5 $\rm M_\odot$ star[2] (see also Armitage 2000). These values agree well with the values for MS stars in our model (see Fig. 3). We also note that Parravano et al. (2003) indirectly verified their models by comparing them with observed interstellar FUV radiation fields.

[2] In Parravano et al. (2003), $L_{\rm FUV,ph}$ of $< 1.8\,\rm M_\odot$ stars and $\Phi_{\rm EUV,ph}$ of $< 5\,\rm M_\odot$ are not available (see their Table 1).

2.3. *Stellar FUV luminosity*

Using the results in Sects. 2.1 and 2.2 and the observational results, we model stellar FUV luminosity $L_{\rm FUV}$. We adopt the same model of $L_{\rm FUV}$ as Gorti et al. (2009) and assume that $L_{\rm FUV}$ is the sum of three components:

$$L_{\rm FUV} = L_{\rm FUV,acc} + L_{\rm FUV,ph} + L_{\rm FUV,chr}\,, \qquad (5)$$

where $L_{\rm FUV,acc}$ is originated from the accretion process, $L_{\rm FUV,ph}$ from the stellar photosphere and $L_{\rm FUV,chr}$ from the stellar chromosphere.

We assume that 4% of the gravitational energy of accreting materials ($= GM_\star\dot{M}_{\rm acc}/R_\star$) is emitted as FUV photons (Calvet & Gullbring 1998) and therefore

$$L_{\rm FUV,acc} = 10^{-2}\,{\rm L}_\odot \left(\frac{M_\star}{\rm M_\odot}\right)\left(\frac{R_\star}{\rm R_\odot}\right)^{-1}\left(\frac{\dot{M}_{\rm acc}}{10^{-8}\,{\rm M_\odot/yr}}\right), \qquad (6)$$

where $\dot{M}_{\rm acc}$ is the mass accretion rate onto the star. Observations also suggest that $L_{\rm FUV}$ of classical T Tauri stars is proportional to $\dot{M}_{\rm acc}$ (e.g., Ingleby et al. 2011). We also adopt the $L_{\rm FUV,chr}$ model as

$$L_{\rm FUV,chr} = 10^{-3.3} L_\star \qquad (7)$$

(see section 3.1 of Alexander et al. 2014, and references therein). We adopt the $L_{\rm FUV,ph}$ model in Sect. 2.2. Because $L_{\rm FUV,acc}$ depends on the initial condition and disk evolution, we will show our $L_{\rm FUV}$ models in Sect. 4. We note that all the components (i.e., $L_{\rm FUV,acc}$, $L_{\rm FUV,ph}$ and $L_{\rm FUV,chr}$) are important (see Fig. 9).

2.4. *Stellar EUV luminosity*

The origin of EUV photons from pre-MS stars remains still unclear, because interstellar hydrogen atoms easily absorb EUV and it is difficult to observationally measure their $\Phi_{\rm EUV}$. In this article we consider EUV from stellar corona and photosphere and assume that $\Phi_{\rm EUV}$ is the sum of them ($\Phi_{\rm EUV,cor}$ and $\Phi_{\rm EUV,ph}$, respectively) as

$$\Phi_{\rm EUV} = \Phi_{\rm EUV,cor} + \Phi_{\rm EUV,ph}\,. \tag{8}$$

We simply adopt $\Phi_{\rm EUV,cor} = 10^{41}\,{\rm s}^{-1}$ in this article (see Sect. 5.4). We adopt the $\Phi_{\rm EUV,ph}$ model in Sect. 2.2.

2.5. *Stellar X-ray Luminosity*

Stellar X-rays are emitted from the hot corona by magnetic activity. Although the accretion onto the star may also contribute to the X-ray luminosity $L_{\rm X}$ (see, e.g., Kastner et al. 2002, 2004), in this paper we neglect this possibility for simplicity (see Sect. 5.4). We model the evolution of $L_{\rm X}$ based on the following two observed features.

First, observations have suggested that $L_{\rm X}$ depends on the stellar Rossby number. The $L_{\rm X}$ of rapid rotators is known to be a function of $L_\star$, that is, the fractional X-ray luminosity ($R_{\rm X} \equiv L_{\rm X}/L_\star$) is constant at around 10^{-3} (e.g., Vilhu & Rucinski 1983). Most T-Tauri stars rotate rapidly and have this relation (so-called "saturation"; Flaccomio et al. 2003; Preibisch et al. 2005; Telleschi et al. 2007). On the other hand, $R_{\rm X}$ of IM stars or slow rotators is more complex. Since the dynamo efficiency depends on both the rotation period and the depth of convective zone, Noyes et al. (1984) and Mangeney & Praderie (1984) introduced the Rossby number, which is the ratio of the rotational period to the convective turnover timescale ($Ro = P_{\rm rot}/\tau_{\rm conv}$), as an indicator of the X-ray activity. Wright et al. (2011) have combined the observed data of both saturated and unsaturated stars and derived the following empirical formula: $R_{\rm X} = \min\left[10^{-3.13}, 5.3\times10^{-6}\,Ro^{-2.7}\right]$. The threshold value of the saturation is ${\rm Ro}_{\rm sat} = 0.16$.

Secondly, $L_{\rm X}$ of pre-MS IM stars depend strongly on their age. Hamaguchi et al. (2005) and Huenemoerder et al. (2009) reported that young IM stars on or leaving their Hayashi track have a high $R_{\rm X}$ ($\sim 10^{-3}$–10^{-4})[3]. On the other hand, the older counterparts, Herbig Ae/Be stars, have smaller values of $R_{\rm X}$ ranging from 10^{-5} to 10^{-7} according to observations (Zinnecker & Preibisch 1994; Hamaguchi et al. 2005; Hamidouche et al. 2008; Stelzer et al. 2009). The strong dependence of $L_{\rm X}$ of IM stars on age (or $T_{\rm eff}$) is shown in Flaccomio et al. (2003); Hamaguchi et al. (2005); Gregory et al. (2016). Flaccomio et al. (2003, see their figure 9) showed that the median value of $L_{\rm X}$ of 2–3 $M_\odot$ stars decrease at around a few Myr by orders of magnitude. We note that this is consistent with recent observations by Villebrun et al. (2019), which have suggested that young IM stars possess magnetic fields, whereas most (90–95%) Herbig Ae/Be stars do not. Therefore, we assume that the evolution of $L_{\rm X}$ of IM stars can also be modeled with the Rossby number: the increase of the Ro number with time results in the $R_{\rm X}$ decrease. Although the physical origin of the weak X-ray emission of Herbig Ae/Be stars is still under debate, we impose a lower limit to $R_{\rm X} = 10^{-7}$ even if $Ro > 4.35 \equiv {\rm Ro}_{\rm floor}$. We note that we confirmed that this floor value has little impact on disk evolution.

Considering the above observational constraints, we model the $L_{\rm X}$ evolution as follows:

$$L_{\rm X} = \max\left[\min\left(10^{-3.13}, 5.3\times10^{-6}\,Ro^{-2.7}\right), 10^{-7}\right] L_\star\,. \tag{9}$$

We note that the choice of the lower limit of $R_{\rm X}(=10^{-7})$ has little impact on disk evolution.

To compute $L_{\rm X}$ with Eq. 9, we need the evolution of $\tau_{\rm conv}$ and $P_{\rm rot}$. From the mixing-length theory (Cox & Giuli 1968), $\tau_{\rm conv}$ in the stellar interior can be estimated as

$$\tau_{\rm conv} = \left[\frac{M_{\rm conv}(R_\star - R_{\rm conv})^2}{3L_\star}\right]^{1/3}, \tag{10}$$

where $M_{\rm conv}$ is the mass in the convective envelope and $R_{\rm conv}$ is the radius at the base of the envelope (Zahn 1977; Rasio et al. 1996; Villaver & Livio 2009).

The $P_{\rm rot}$ value of stars younger than several Myr (corresponding to the disk lifetime) ranges from 1–10 days and is almost constant with time probably due to the star-disk locking (Rebull et al. 2004; Bouvier 2008; Gallet & Bouvier 2013). Therefore we set the fiducial value of $P_{\rm rot}$ to be 3 days and investigate the influence of its variation in Sect. 5.2.

Figures 4a and 4b show the time evolutions of $L_\star$ and Ro, respectively. Figure 5 shows our model of the $L_{\rm X}$

[3] We note that we should be careful on the contribution by an unresolved binary star, but Hamidouche et al. (2008) ruled out this possibility with an 80% confidence level.

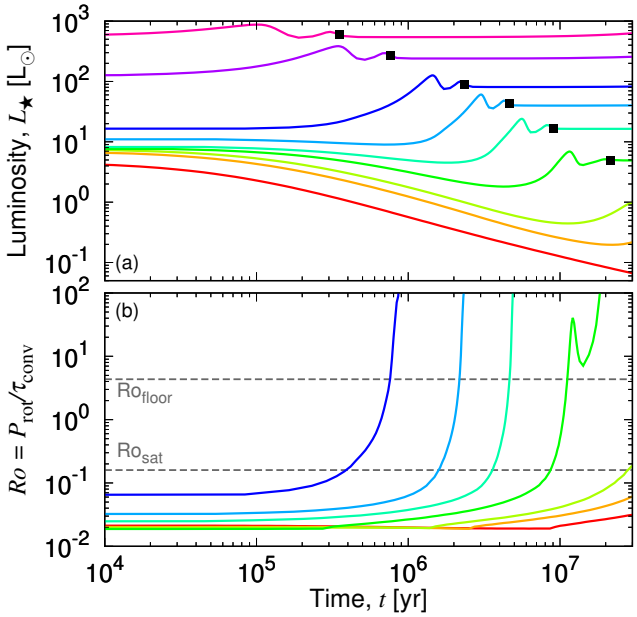

Figure 4. *Top panel.* Evolution of $L_\star$ of 0.5–5 $M_\odot$ stars (from bottom to top; color-coded by stellar mass as curves in Fig. 1). The squares denote the ZAMS. *Bottom panel.* Evolution of Ro ($= P_{rot}/\tau_{conv}$) of 0.5–3 $M_\odot$ (from bottom to top) with $P_{rot} = 3$ days. The dashed lines show the critical Rossby numbers ($Ro_{sat} = 0.16$ and $Ro_{floor} = 4.35$). We note that 4 and 5 $M_\odot$ stars have a large Ro from the beginning.

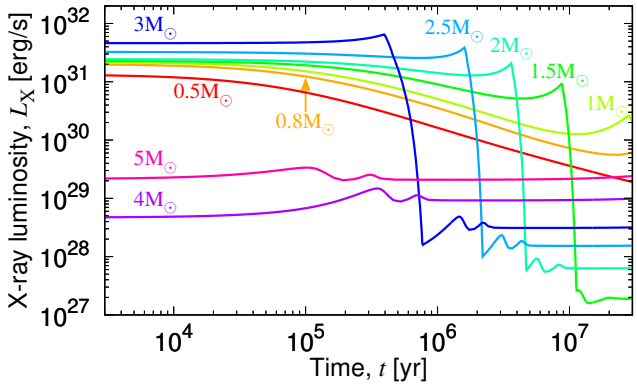

Figure 5. Evolution of L_X of 0.5–5 $M_\odot$ stars.

evolution combining Eq. 9 and Fig. 4. One might be skeptical about our prescription of L_X. We compare our model of L_X over time with observational data in Gregory et al. (2016, see their Fig. C2). Figure 6 shows that our model of the L_X evolution is in good agreement with the data in Gregory et al. (2016). The observed L_X data show that 0.5–1 $M_\odot$ stars have the gradual decrease for ~ 10 Myr, whereas $\geq 1.5\,M_\odot$ stars have the decrease by orders of magnitude. Our model captures such features and the L_X values and the timing of decrease are also reproduced. We have also confirmed that our model is consistent with Flaccomio et al. (2003); Güdel (2004) and the Sun[4]. We admit, however, that Fig. 6 shows that the L_X values of 1–1.5 $M_\odot$ in our model are several times larger than the median value of the observed L_X. Moreover, the observed R_X has a large scatter (~ 1 dex; e.g., Preibisch et al. 2005). We will investigate the impact of the larger/smaller value of L_X in Sect. 5.2.

Our stellar evolutionary models described in Sect. 2 are provided in Table 1.

3. PHYSICAL MODEL AND COMPUTATION METHOD OF DISK EVOLUTION

We simulate the time evolution of protoplanetary disks including the effects of viscous accretion and the time-dependent PE (Sect. 3.1). We adopt the PE models from the literature (Sect. 3.2), considering stellar evolution on the pre-MS (see Sect. 2). The criterion for the disk dispersal is described in Sect. 3.3. The numerical method and computational settings are summarized in Sect. 3.4.

3.1. *Basic equations*

We solve the one-dimensional diffusion equation for the surface density profile (e.g., Lynden-Bell & Pringle 1974; Clarke et al. 2001):

$$\frac{\partial \Sigma}{\partial t} = \frac{3}{R}\frac{\partial}{\partial R}\left[\sqrt{R}\frac{\partial}{\partial R}\left(\nu_{vis}\Sigma\sqrt{R}\right)\right] - \dot{\Sigma}_{PE}(R,t)\,, \quad (11)$$

where Σ is the surface density, t the time, R the distance from the central star, ν_{vis} the viscosity, and $\dot{\Sigma}_{PE}$ the PE rate, under the cylindrical coordinates (R, ϕ, z).

We adopt the viscosity model of Shakura & Sunyaev (1973): $\nu_{vis} = (2/3)\alpha c_s^2/\Omega$, where c_s is the sound speed at the disk midplane and Ω the angular velocity. We neglect the disk self-gravity and pressure gradient force and adopt $\Omega = \sqrt{GM_\star/R^3}$, where G is the gravitational constant.

For the midplane temperature T_{mid}, we consider both the viscous heating and stellar irradiation, following Kunitomo et al. (2020, see their Sect. 2.2), which is based on Suzuki et al. (2016). Since in this paper we consider the $L_\star$ evolution (see Sect. 2), the disk temperature in the entire region evolves with time because both viscous heating and stellar irradiation change with time. We define $c_s^2 = k_B T_{mid}/(\mu m_u)$, where k_B is the Boltzmann

[4] The Sun has $M_{conv} = 0.025\,M_\odot$ and $R_{conv} = 0.713\,R_\odot$ (Bahcall et al. 2005) and therefore $\tau_{conv,\odot} = 13.9$ days. Combining this with $P_{rot} \simeq 26.9$ days, $Ro_\odot \simeq 1.94$. Equation (9) with $Ro_\odot = 1.94$ gives $R_X = 8.9\times10^{-7}$, which is consistent with the observed solar value, $R_{X,\odot} \simeq 10^{-7}$–$10^{-6}$ (Judge et al. 2003).

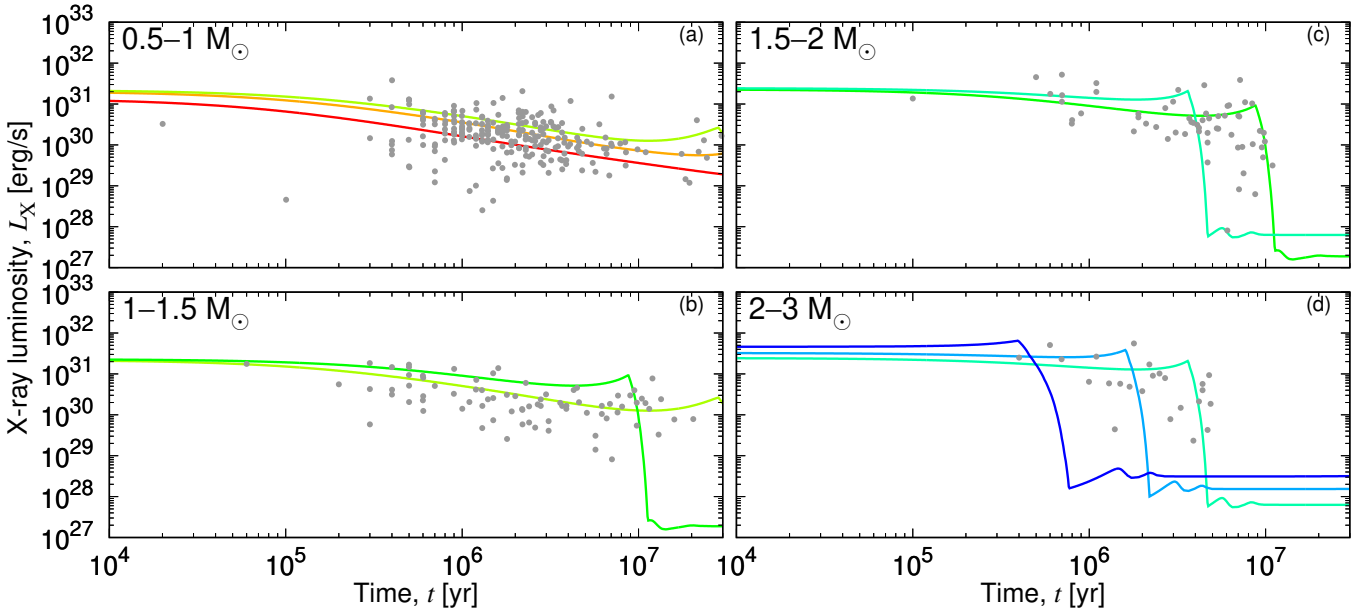

Figure 6. Comparison of our L_X evolutionary models of 0.5, 0.8, 1, 1.5, 2, 2.5 and 3 $M_\odot$ stars (the solid lines; same as Fig 5) and the observed data (points; Gregory et al. 2016) in the range of 0.5–1 $M_\odot$ (left top panel), 1–1.5 $M_\odot$ (left bottom), 1.5–2 $M_\odot$ (right top) and 2–3 $M_\odot$ (right bottom).

Table 1. Stellar evolutionary models.

$M_\star$ [$M_\odot$]	$\log t$ [yr]	$R_\star$ [$R_\odot$]	$L_\star$ [$L_\odot$]	$T_{\rm eff}$ [K]	$M_{\rm conv}$ [$M_\odot$]	$R_{\rm conv}$ [$R_\odot$]	$\tau_{\rm conv}$ [day]	L_X [erg/s]	$\Phi_{\rm EUV,ph}$ [1/s]	$L_{\rm FUV,ph}$ [erg/s]
0.5	0.00	4.537E+00	4.883E+00	4.032E+03	5.000E-01	5.113E-02	1.387E+02	1.391E+31	0.000E+00	1.162E+26
0.5	1.00	4.536E+00	4.686E+00	3.991E+03	4.998E-01	1.858E-01	1.377E+02	1.335E+31	0.000E+00	8.965E+25
0.5	2.00	4.536E+00	4.685E+00	3.991E+03	4.998E-01	1.858E-01	1.377E+02	1.334E+31	0.000E+00	8.964E+25
⋮										

Continued

NOTE—Evolutionary models of young 0.5–5 $M_\odot$ stars. Table 1 is published in its entirety in the machine-readable format. A portion is shown here for guidance regarding its form and content.

constant, $\mu = 2.34$ the mean molecular weight and m_u the atomic mass unit.

3.2. *Photoevaporation Models*

In this paper we consider the PE driven by the irradiation from a central star (so-called "internal PE") and do not consider the external irradiation by a nearby massive star (e.g., Adams et al. 2004; Haworth & Clarke 2019).

So far a number of studies have been performed on the internal PE (e.g., Hollenbach et al. 1994; Font et al. 2004; Ercolano et al. 2008; Gorti & Hollenbach 2009; Tanaka et al. 2013; Komaki et al. 2020). We also refer the reader to the recent reviews such as Alexander et al. (2014); Gorti et al. (2016); Ercolano & Pascucci (2017).

We consider the PE driven by FUV, EUV and X-rays and we adopt their mass-loss rates from the literature. We assume that the dominant heating source among the three at the wind launching region determines the mass-loss rate $\dot{\Sigma}_{\rm PE}$ and therefore

$$\dot{\Sigma}_{\rm PE}(R,t) = \max\left[\dot{\Sigma}_{\rm FUV}(R,t), \dot{\Sigma}_{\rm EUV}(R,t), \dot{\Sigma}_{\rm X}(R,t)\right], \quad (12)$$

where $\dot{\Sigma}_{\rm FUV}, \dot{\Sigma}_{\rm EUV}$ and $\dot{\Sigma}_{\rm X,0}$ are the PE rate driven by FUV, EUV and X-rays, respectively. We note that one might think that $\dot{\Sigma}_{\rm PE}$ can be proportional to the total energy deposited in the disk atmosphere and therefore $\dot{\Sigma}_{\rm PE} = \dot{\Sigma}_{\rm FUV} + \dot{\Sigma}_{\rm EUV} + \dot{\Sigma}_{\rm X}$. We have confirmed that the two expressions of $\dot{\Sigma}_{\rm PE}$ make little difference in the

results ($< 8\%$ in disk lifetime), because almost always one process among the three dominates.

The PE rate has two regimes: one is for primordial disks and the other is for disks with an inner hole. In the latter, the outer disk is directly irradiated and therefore the PE profile is changed (so-called "direct PE"). We consider both regimes.

We adopt the same $\dot{\Sigma}_{\rm EUV}$ model as in Kunitomo et al. (2020); $\dot{\Sigma}_{\rm EUV}$ for primordial disks in Alexander & Armitage (2007) and that for the direct PE in Alexander et al. (2006b). The total mass-loss rates for the EUV PE in the both regimes are

$$\dot{M}_{\rm EUV,p} = 1.6\times10^{-10}\,{\rm M}_\odot/{\rm yr}\left(\frac{\Phi_{\rm EUV}}{10^{41}{\rm s}^{-1}}\right)^{1/2}\left(\frac{M_\star}{1{\rm M}_\odot}\right)^{1/2} \quad (13)$$

and

$$\dot{M}_{\rm EUV,d} = 1.3\times10^{-9}\,{\rm M}_\odot/{\rm yr}\left(\frac{\Phi_{\rm EUV}}{10^{41}{\rm s}^{-1}}\right)^{1/2}\left(\frac{R_{\rm hole,EUV}}{3\,{\rm au}}\right)^{1/2}, \quad (14)$$

where $\Phi_{\rm EUV}$ is the EUV photon luminosity and $R_{\rm hole,EUV}$ is the inner hole size for EUV. We assume the aspect ratio $h/R = 0.05$ in Eq. (14) (see Alexander et al. 2006b), where $h = \sqrt{2}c_s/\Omega$ is the gas scale height[5]. The $\dot{\Sigma}_{\rm EUV}$ profile of primordial disks have a peak at $\simeq 1\,{\rm au}\,(M_\star/{\rm M}_\odot)$. We refer the reader to Alexander & Armitage (2007) for the full formula of $\dot{\Sigma}_{\rm EUV}$ (see also Fig. 7).

As for the X-ray PE rate, the prescription in Owen et al. (2012) has been widely used. In the case of a $1\,{\rm M}_\odot$ star with $L_{\rm X} = 10^{30}\,{\rm erg/s}$, $\dot{\Sigma}_{\rm X}$ has a peak value ($\equiv \dot{\Sigma}_{\rm X,0} = 5.1\times10^{-12}\,{\rm g\,s^{-1}\,cm^{-2}}$) at $2.5\,{\rm au}\,(M_\star/{\rm M}_\odot)$[6], decreases with radius as R^{-2}, and has a sharp cutoff at several tens of au. The cutoff is however not seen in the recent study by Picogna et al. (2019, see their Fig. 5). For the primordial disks, we adopt

$$\dot{\Sigma}_{\rm X} = \dot{\Sigma}_{\rm X,0}\left(\frac{L_{\rm X}}{10^{30}\,{\rm erg/s}}\right)\left(\frac{R}{2.5\,{\rm au}}\right)^{-2}, \quad (15)$$

outside $2.5\,{\rm au}(M_\star/{\rm M}_\odot)$. In the inner region the disk gas is gravitational bound to the disk and does not flow out (i.e., $\dot{\Sigma}_{\rm X} = 0$). We note that we neglect the weak dependence on stellar mass ($\propto M_\star^{-0.068}$) in the original $\dot{\Sigma}_{\rm X}$ profile in Owen et al. (2012). We note that the X-ray PE rate in Owen et al. (2012) has recently been called into question; the radiation-hydrodynamic (RHD hereafter) simulations with self-consistent thermochemistry by Wang & Goodman (2017); Nakatani et al. (2018a) disagree with the results in Owen et al. (2012) and therefore Eq. (15) may overestimate the X-ray PE rate (see also a pioneering study by Gorti & Hollenbach 2009). We will discuss this issue in Sect. 5.4.

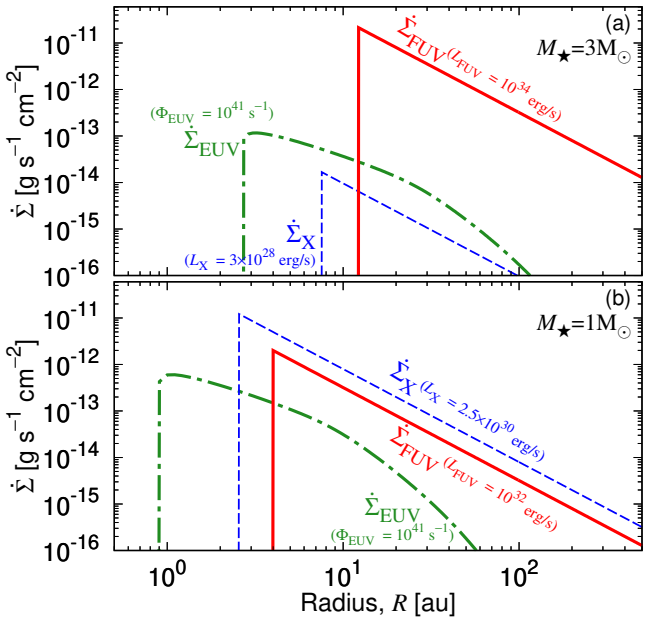

Figure 7. Examples of mass-loss profiles by FUV (solid red; $\dot{\Sigma}_{\rm FUV}$), EUV (dot-dashed green; $\dot{\Sigma}_{\rm EUV}$) and the X-ray (the dotted blue line; $\dot{\Sigma}_{\rm X}$) in the case of a disk without an inner hole. Top and bottom panels show the cases around a $3\,{\rm M}_\odot$ star with $L_{\rm FUV} = 10^{34}\,{\rm erg/s}$, $\Phi_{\rm EUV} = 10^{41}\,{\rm s}^{-1}$ and $L_{\rm X} = 3\times10^{28}\,{\rm erg/s}$, and around a $1\,{\rm M}_\odot$ star with $L_{\rm FUV} = 10^{32}\,{\rm erg/s}$, $\Phi_{\rm EUV} = 10^{41}\,{\rm s}^{-1}$ and $L_{\rm X} = 2.5\times10^{30}\,{\rm erg/s}$, respectively. Since those luminosities evolve with time, these profiles are just an example.

For $\dot{\Sigma}_{\rm X}$ of the direct PE, we adopt the model in Owen et al. (2012, see their appendix B), which peaks at the inner edge of the outer disk. The total mass-loss rate is

$$\dot{M}_{\rm X,d} = 4.8\times10^{-9}\,{\rm M}_\odot/{\rm yr}\left(\frac{L_{\rm X}}{10^{30}\,{\rm erg/s}}\right)^{1.14}\left(\frac{M_\star}{{\rm M}_\odot}\right)^{-0.148}, \quad (16)$$

where the subscript "d" stands for the direct PE.

We need to define the inner hole sizes for the direct PE for EUV and X-rays. We also modify $\dot{\Sigma}_{\rm EUV}$ and $\dot{\Sigma}_{\rm X}$ for the direct PE to avoid numerical problems using "smoothing functions". We refer readers to Kunitomo et al. (2020, see their Sect. 2.4) for the full details of these prescriptions.

As for the $\dot{\Sigma}_{\rm FUV}$ model, no formula is available to date in the literature. We construct the $\dot{\Sigma}_{\rm FUV}$ model as a function of R and the stellar FUV luminosity $L_{\rm FUV}$,

[5] We note that sometimes the factor of $\sqrt{2}$ is not included. We include it following Kunitomo et al. (2020).

[6] The peak of the X-ray PE (at 2.5 au for a $1\,{\rm M}_\odot$ star) is outer than that the EUV PE (at 1 au), because the X-ray PE is launched from the atomic layer ($\simeq$ 3000–5000 K), whereas the EUV PE is from the 10^4 K layer (Alexander et al. 2014).

based on the results in Gorti & Hollenbach (2009) and Wang & Goodman (2017). The latter performed RHD simulations, whereas the former conducted calculations using a hydrostatic model.

Gorti & Hollenbach (2009) investigated the dependence of $\dot{\Sigma}_{\rm FUV}$ on $L_{\rm FUV}$ (see Model F10, S and F0.1 in their Fig. 4) around a $1\,{\rm M}_\odot$ star. The $\dot{\Sigma}_{\rm FUV}$ value beyond 4 au changes by about one order of magnitude by varying $L_{\rm FUV}$ by an order of magnitude. Therefore we assume that $\dot{\Sigma}_{\rm FUV} \propto L_{\rm FUV}$ and the FUV PE mass loss occurs beyond $4\,{\rm au}\,(M_\star/{\rm M}_\odot)$. We note that 4 au corresponds to the critical radius for $\simeq 2000\,{\rm K}$ gas around a $1\,{\rm M}_\odot$ star (Liffman 2003). The gas heated by FUV is much cooler than that by EUV, which is $\simeq 10^4\,{\rm K}$ (see also Nakatani et al. 2018b).

The $\dot{\Sigma}_{\rm FUV}$ profile in Gorti & Hollenbach (2009) is a complex function of R (see their Fig. 4), whereas Wang & Goodman (2017) claims that $2\pi R^2 \dot{\Sigma}_{\rm FUV}$ is almost constant (see their Fig. 8). Wang & Goodman (2017, see their Sect. 5.2) confirmed that the difference arises from how to estimate the mass-loss rate: The sonic point is different between the hydrodynamic simulations in Wang & Goodman (2017) and the hydrostatic models in Gorti & Hollenbach (2009). The $\dot{\Sigma}_{\rm FUV} \propto R^{-2}$ profile seems energetically reasonable. Therefore, from the results in Wang & Goodman (2017), we assume that $\dot{\Sigma}_{\rm FUV} \propto R^{-2}$ and $\dot{\Sigma}_{\rm FUV} = 10^{-12}\,{\rm g\,cm^{-2}\,s^{-1}} (\equiv \dot{\Sigma}_{\rm FUV,0})$ at 4 au around a $1\,{\rm M}_\odot$ star. As a result, we adopt the following $\dot{\Sigma}_{\rm FUV}$ profile: in the outer disk beyond $4\,{\rm au}\,(M_\star/{\rm M}_\odot)$,

$$\dot{\Sigma}_{\rm FUV} = \dot{\Sigma}_{\rm FUV,0} \left(\frac{L_{\rm FUV}}{10^{31.7}\,{\rm erg/s}} \right) \left(\frac{R}{4\,{\rm au}} \right)^{-2}, \qquad (17)$$

and in the inner disk ($R < 4{\rm au}\,(M_\star/{\rm M}_\odot)$), $\dot{\Sigma}_{\rm FUV} = 0$.

Figure 7 shows examples of the $\dot{\Sigma}_{\rm PE}$ profiles of two cases; one is around a $3\,{\rm M}_\odot$ star with $L_{\rm FUV} = 10^{34}\,{\rm erg/s}$, $\Phi_{\rm EUV} = 10^{41}\,{\rm s^{-1}}$ and $L_{\rm X} = 3\times10^{28}\,{\rm erg/s}$, and the other is around a $1\,{\rm M}_\odot$ star with $L_{\rm FUV} = 10^{32}\,{\rm erg/s}$, $\Phi_{\rm EUV} = 10^{41}\,{\rm s^{-1}}$ and $L_{\rm X} = 10^{31}\,{\rm erg/s}$. As described in Sect. 2, these luminosities evolve with time and therefore the PE rate varies with time.

3.3. *Disk dispersal criterion*

In this study we define the time when the disk mass, $M_{\rm disk}$, decreases down to $10^{-8}\,M_{\rm d,ini}$ as the disk lifetime, $t_{\rm disk}$, where $M_{\rm d,ini}$ is the initial disk mass. Here we take a numerical factor 10^{-8} but $t_{\rm disk}$ is insensitive to it, if it is $\leq 10^{-4}$.

We note that Kimura et al. (2016); Kunitomo et al. (2020) measured the inner disk lifetime when the optical depth of the inner disk (i.e., IR-emitting region) becomes unity. Considering the fact that the IR is emitted by dust grains which are not modeled in this study (see Sect. 5.4), here we measure $t_{\rm disk}$ using $M_{\rm disk}$. However, we note that the inner disk lifetime using the optical depth is almost the same as $t_{\rm disk}$ in this study, because an entire disk disperses quickly once a gap opens (see Fig. 8a).

3.4. *Numerical method*

We numerically solve Eq. (11) using the time-explicit method based on Kunitomo et al. (2020). The calculation domain ranges from 0.01 to 10^4 au. The grid size is in proportion to $\sqrt{R}$ and the number of mesh points is 2000. The zero-torque boundary condition is imposed at both the inner and outer boundaries. We measure $\dot{M}_{\rm acc}$ at the innermost cell. We stop calculations when the disk is completely dispersed.

We adopt the self-similar solution (Lynden-Bell & Pringle 1974) as an initial surface density profile given by

$$\Sigma(R, t=0) = \frac{M_{\rm d,ini}}{2\pi R_1^2} \frac{\exp\left(-R/R_1\right)}{R/R_1}. \qquad (18)$$

The characteristic radius R_1 represents the location outside which the e^{-1} of the disk mass resides.

We choose input parameters to reproduce observational constraints as summarized in Table 2. First, from the observed relation that disk masses are proportional to $M_\star$ (e.g., Williams & Cieza 2011; Andrews et al. 2013; Mohanty et al. 2013; Pascucci et al. 2016), we adopt

$$M_{\rm d,ini} \propto M_\star\,. \qquad (19)$$

The proportionality factor ranges from 0.001–0.1. Given that this value decreases with time, we start calculations with a massive disk, $M_{\rm d,ini} = 0.1\,M_\star$ (i.e., from the early phase). We note that the quantity of $M_{\rm d,ini}/M_\star$ does not change the qualitative results on the disk lifetimes.

Secondly, following Gorti et al. (2009), we adopt

$$\alpha \propto M_\star \qquad (20)$$

in order to reproduce the observed relation $\dot{M}_{\rm acc} \propto M_\star^2$ (e.g., Calvet et al. 2004; Muzerolle et al. 2005). We assume that magnetorotational instability (MRI hereafter; Velikhov 1959; Chandrasekhar 1961; Balbus & Hawley 1991) is the source of the turbulent viscosity and we adopt $\alpha = 10^{-2}\,(M_\star/{\rm M}_\odot)$. Equation (20) is derived with the following assumptions: the steady-state accretion ($\dot{M}_{\rm acc} = 3\pi\Sigma\nu_{\rm vis}$), the constant R_1 with $M_\star$ and Eq. (19) (therefore $\Sigma \propto M_\star$), the optically-thin disk temperature (see, e.g., Eq. 6 of Kunitomo et al. 2020), $L_\star \propto M_\star^2$ (see $L_\star$ at 1 Myr in Fig. 4a or Siess et al. 2000), and the Keplerian Ω.

Finally, we adopt the initial disk radius $R_1 = 50$ au. Andrews et al. (2010) measured dust disk radii from

Table 2. Fiducial disk model.

Parameter	Value
Initial disk mass $M_{\rm d,ini}$	$0.1\,M_\star$
Viscosity parameter α	$10^{-2}(M_\star/{\rm M}_\odot)$
Initial characteristic radius R_1	50 au
Coronal EUV luminosity $\Phi_{\rm EUV,cor}$	$10^{41}\,{\rm s}^{-1}$

millimeter wavelength observations and found that it ranges from 14 to 200 au and peaks at ~ 30 au (see their figure 3). Considering that recent studies have suggested that gas disks are likely to be larger than dust disks (e.g., Ansdell et al. 2018), we adopt $R_1 = 50$ au in this paper. Andrews et al. (2010) did not find a clear correlation between the disk radius and $M_\star$ (see also Ansdell et al. 2018; Long et al. 2019). Although recently Andrews et al. (2018) have suggested a weak correlation with $M_\star$, in this article we adopt the constant R_1 with $M_\star$ for simplicity.

4. RESULTS

4.1. *Overview of disk evolution*

In this subsection we show the disk evolution around a $3\,{\rm M}_\odot$ star with the fiducial settings listed in Table 2. In our results $t = 0$ corresponds to the time when stars appear on their birthline. We consider the three PE mechanisms: FUV, EUV and X-rays. In the four panels of Fig. 8, we show the evolution of (a) the Σ profile, (b) the $T_{\rm mid}$ profile, (c) $\dot{M}_{\rm acc}$ and the mass-loss rates and (d) the time-integrated accreted or lost mass. We define $\dot{M}_{\rm FUV} \equiv \int 2\pi R \dot{\Sigma}_{\rm FUV} dR$ and $\dot{M}_{\rm X} \equiv \int 2\pi R \dot{\Sigma}_{\rm X} dR$ (see Eqs. 15 and 17). Both are integrated over the entire computation domain. The time-integrated accreted mass is $M_{\rm acc} \equiv \int \dot{M}_{\rm acc} dt$, and the total mass lost by the PE is $M_{\rm PE} \equiv \int \dot{\Sigma}_{\rm PE} dR dt$ (see Eq. 12). We note that we have checked the mass conservation in our simulations: $M_{\rm d,ini} = M_{\rm disk}(t) + M_{\rm acc}(t) + M_{\rm PE}(t)$ with a precision of $< 10^{-10}$.

The qualitative behavior of the evolution in Fig. 8 is the same as the results in previous works (e.g., Clarke et al. 2001; Alexander et al. 2006a; Gorti et al. 2009; Owen et al. 2010): (i) $M_{\rm disk}$ decreases with time due to viscous accretion, (ii) a gap is created when and where the accretion rate decreases down to the PE rate, (iii) the inner disk depletes in the viscous timescale at the gap, and then (iv) after the dispersal of the inner disk, the outer disk is directly irradiated and also quickly dispersed. The gap opens at ~ 15 au, slightly outside the peak of $\dot{\Sigma}_{\rm FUV}$ (see Sect. 3.2). We note that the period of the phase (iii) is consistent with the viscous timescale, $\tau_{\rm vis}$, at the gap given by

$$\tau_{\rm vis} \equiv \frac{R^2}{\nu_{\rm vis}} \tag{21}$$
$$= 0.07\,{\rm Myr}\left(\frac{R}{15\,{\rm au}}\right)^{1/2}\left(\frac{T_{\rm mid}}{100\,{\rm K}}\right)^{-1}\left(\frac{M_\star}{3\,{\rm M}_\odot}\right)^{1/2}\left(\frac{\alpha}{0.03}\right)^{-1}.$$

We note the non-smooth $T_{\rm mid}$ profile in Fig. 8b results from the non-linear function of the opacity (see Kunitomo et al. 2020).

Figure 8c shows that the mass-loss rates evolve with time, unlike the previous studies. Although the X-ray PE rate, $\dot{M}_{\rm X}$, is high (a few $10^{-7}\,{\rm M}_\odot$/yr) in the early phase, $\dot{M}_{\rm X}$ decreases by more than three orders of magnitude between 0.3 and 0.7 Myr. This is induced by stellar evolution: at this phase, a $3\,{\rm M}_\odot$ star develops a large radiative core, Ro increases, and therefore $L_{\rm X}$ and $\dot{M}_{\rm X}$ decrease (see Figs. 4b and 5). Instead, $\dot{M}_{\rm FUV}$ rapidly increases by more than one order of magnitude at $\simeq 1$ Myr. This is because, after $\simeq 1$ Myr, $T_{\rm eff} > 7300$ K and $L_{\rm FUV,ph}/L_\star > 10^{-2}$, that is, the stellar surface becomes hot enough to emit FUV from the photosphere. We stress that although Gorti et al. (2009) has already found that the rapid disk dispersal around IM stars induced by the PE driven by photospheric UV, they have not considered stellar evolution (see Sect. 4.2). Since the rapid increase of $\dot{M}_{\rm FUV}$ has a strong impact on the disk evolution, we claim that stellar evolution is crucial for the disk dispersal around IM stars.

Figure 9 shows the evolution of $L_{\rm FUV}$ in the cases of $M_\star = 1\,{\rm M}_\odot$ and $3\,{\rm M}_\odot$. The disk evolution around a $1\,{\rm M}_\odot$ star is shown in Appendix B. In the $1\,{\rm M}_\odot$ case, $L_{\rm FUV,acc}$ dominates in the almost entire phase, which is consistent with observations (see, e.g., Ingleby et al. 2011) and previous theoretical study (Gorti et al. 2009). Along with the decrease in $\dot{M}_{\rm acc}$, $L_{\rm FUV}$ decreases with time, and in the late phase, $L_{\rm FUV,chr}$ dominates. In the case of $3\,{\rm M}_\odot$ stars, however, although $L_{\rm FUV,acc}$ dominates in the early phase, $L_{\rm FUV,ph}$ rapidly increases by orders of magnitude as $T_{\rm eff}$ increases at $\simeq$ 1–1.5 Myr. We note that, in the $4\,{\rm M}_\odot$ case the switch occurs at 4×10^4 yr, and in the $5\,{\rm M}_\odot$ case $L_{\rm FUV,ph}$ always dominates.

We note that the initial value of $L_{\rm FUV,acc}$ of the $3\,{\rm M}_\odot$ star is $\simeq 1$ order of magnitude larger than that of $1\,{\rm M}_\odot$. This is because we adopt the initial condition to reproduce the observed relation $\dot{M}_{\rm acc} \propto M_\star^2$ (see Sect. 3.4).

4.2. *Importance of stellar evolution*

In Sect. 4.1, we showed that the photospheric FUV radiation has a dominant role in the disk dispersal around a $3\,{\rm M}_\odot$ star. We again note that it has already been found by Gorti et al. (2009), and as an up-

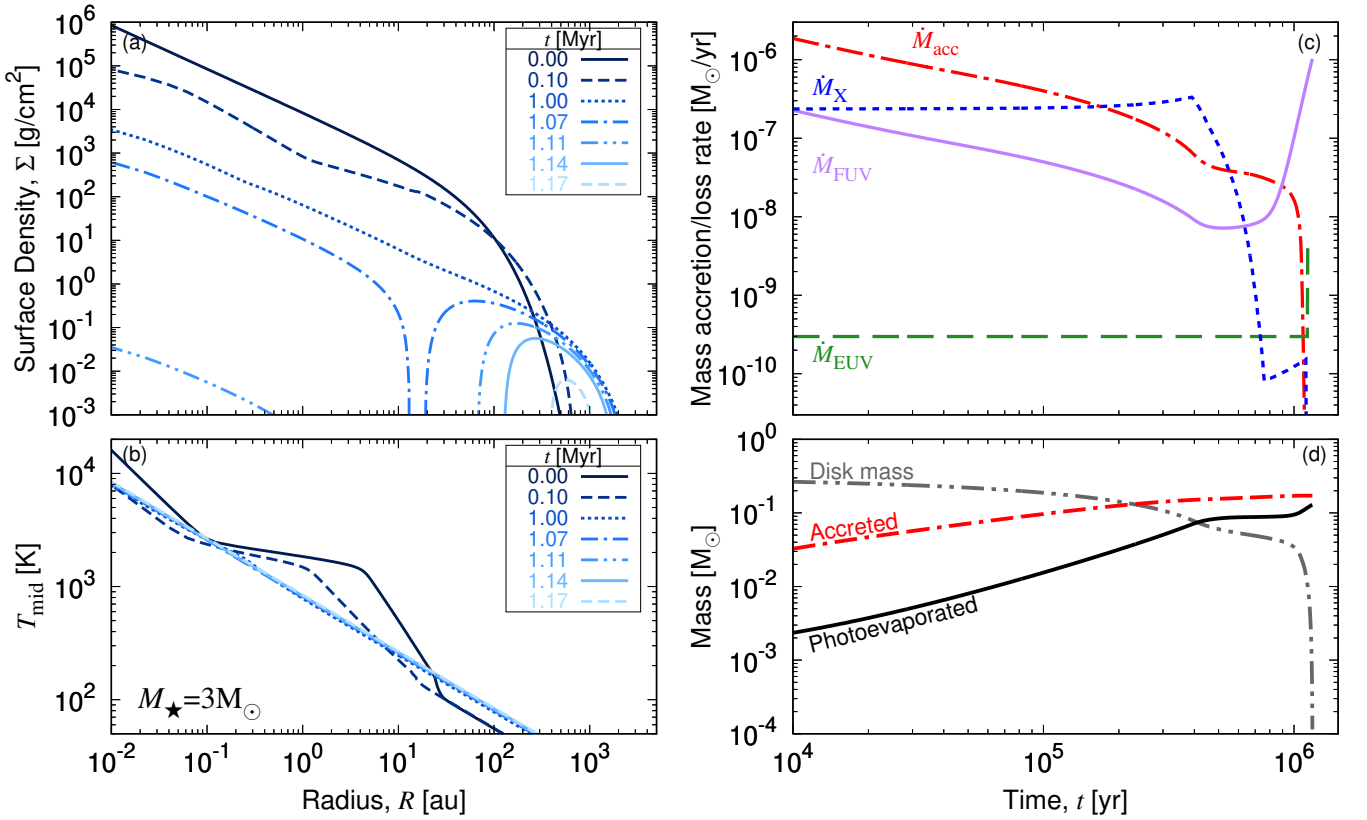

Figure 8. Temporal evolution of a disk around a $3\,M_\odot$ star. The panels (a) and (b) show the evolution of the surface density (Σ) profile and the midplane temperature ($T_{\rm mid}$) profile, respectively. Each line shows a snapshot between 0 and 1.16 Myr. The panel (c) shows the evolution of the mass accretion rate ($\dot{M}_{\rm acc}$, the dot-dashed line) and the mass-loss rate by the X-ray PE ($\dot{M}_{\rm X}$, dotted), the EUV PE ($\dot{M}_{\rm EUV}$, dashed) and the FUV PE ($\dot{M}_{\rm FUV}$, solid). The panel (d) shows the evolution of disk mass ($M_{\rm disk}$, the double dot-dashed line), the time-integrated masses of accretion ($M_{\rm acc}$, dot-dashed) and photoevaporation ($M_{\rm PE}$, solid).

date from their study, we considered the stellar evolution. To illustrate its importance, we performed the same simulation of Fig. 8 but without time evolution of $L_{\rm FUV,ph}, \Phi_{\rm EUV}$ and $L_{\rm X}$ as Gorti et al. (2009). We adopt $L_{\rm FUV,ph} = 1.1 \times 10^{35}$ erg/s, $\Phi_{\rm EUV} = 1.0 \times 10^{39}$ erg/s and $L_{\rm X} = 5.0 \times 10^{28}$ erg/s following Gorti et al. (2009) (see also Sect. 2.1). Figure 10 shows that $\dot{M}_{\rm FUV}$ is kept high from the beginning and therefore the disk disperses much earlier than the case in Fig. 8. As shown in Fig. 9, $L_{\rm FUV}$ of a pre-MS $3\,M_\odot$ star should be much lower than that of a MS star, but, in approaching to their MS, suddenly increases by orders of magnitude. This time evolution has a strong impact on the disk lifetime. We note that Eq. (5) is adopted but always $L_{\rm FUV,ph}$ dominates and therefore $L_{\rm FUV}$ is almost constant with time.

The fact that a disk is dispersed mainly by the PE driven by $L_{\rm FUV,ph}$ is the same in both cases in Figs. 8 and 10. However, for a realistic disk evolution model around IM stars, we claim that stellar evolution is one important ingredient.

We note the difference between the results in Fig. 10 and Gorti et al. (2009): even though the $L_{\rm FUV,ph}, \Phi_{\rm EUV}$ and $L_{\rm X}$ values are the same, the disk lifetimes differ by about one order of magnitude (0.2 Myr and 4 Myr, respectively). We speculate that the difference probably **originates** from the absorption of high-energy photons in disk winds from an inner disk. Gorti et al. (2009, see their section 2.4.1) considered this effect, whereas we do not. This effect can suppress the PE rate in the early phase. We will discuss this issue in Sect. 5.4. Nevertheless, our claim that the time-dependent $L_{\rm FUV,ph}$ is important for disk evolution is still valid.

4.3. *Disk lifetime*

We perform a suite of disk evolution simulations around 0.5–5 $M_\odot$ stars as in Sect. 4.1. We find that $t_{\rm disk}$ decreases with increasing $M_\star$ (Fig. 11a).

To understand which mechanism plays the dominant role, we also perform three sets of simulations (i) with only the FUV PE, (ii) with only the X-ray PE and (iii) without the EUV PE. The other settings are the same

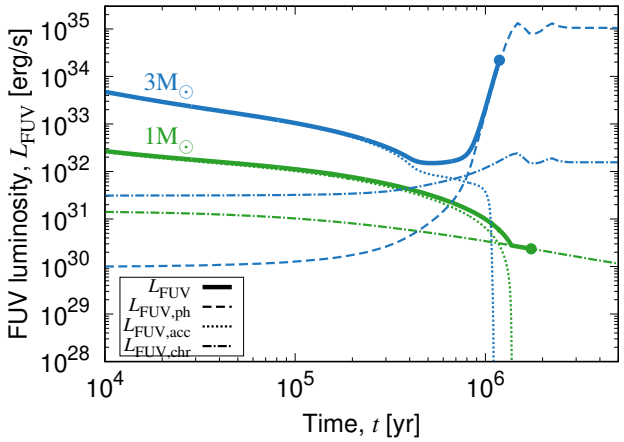

Figure 9. Temporal evolution of $L_{\rm FUV}$ (the thick solid line), $L_{\rm FUV,ph}$ (dashed), $L_{\rm FUV,acc}$ (dotted) and $L_{\rm FUV,chr}$ (dot-dashed) in the cases of $M_\star = 3\,{\rm M}_\odot$ (blue) and $1\,{\rm M}_\odot$ (green). The disks disperse and the simulations stop at the filled circles. We note that $L_{\rm FUV,ph}$ of a $1\,{\rm M}_\odot$ star is negligibly low.

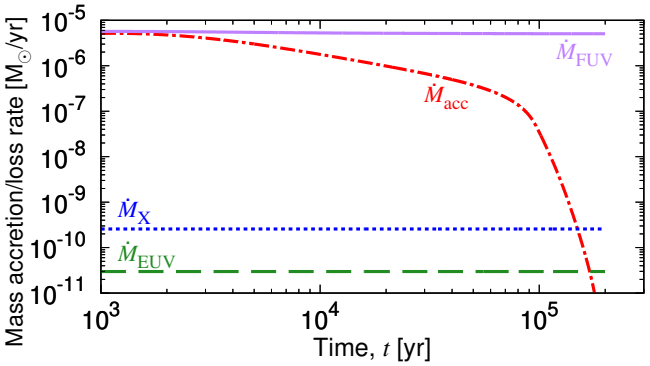

Figure 10. Same as Fig. 8c but with the constant $L_{\rm FUV,ph}(= 1.1 \times 10^{35}\,{\rm erg/s}), \Phi_{\rm EUV}(= 1.0 \times 10^{39}\,{\rm erg/s})$, and $L_{\rm X}(= 5.0 \times 10^{28}\,{\rm erg/s})$ with time. Although $\dot{M}_{\rm FUV}$ changes with time due to the $L_{\rm FUV,acc}$ evolution, it is negligibly small.

as the fiducial runs (see Table 2). In the models where we do not include the FUV and EUV PE (the "only X" model in Fig. 11), the disk lifetime around $\geq 3\,{\rm M}_\odot$ stars increases significantly, while any combination of mechanisms which includes FUV causes similarly short lifetimes for $\geq 3\,{\rm M}_\odot$ stars. These results clearly illustrate that disks around $\geq 3\,{\rm M}_\odot$ stars are dispersed mainly by the FUV PE.

Figure 11b shows the evolution of $M_{\rm disk}$ around a $3\,{\rm M}_\odot$ star. After the X-ray PE becomes less effective at 0.4 Myr, it takes time for the FUV PE to become strong at 1.0 Myr, and then the disks quickly disperse if the FUV PE is considered.

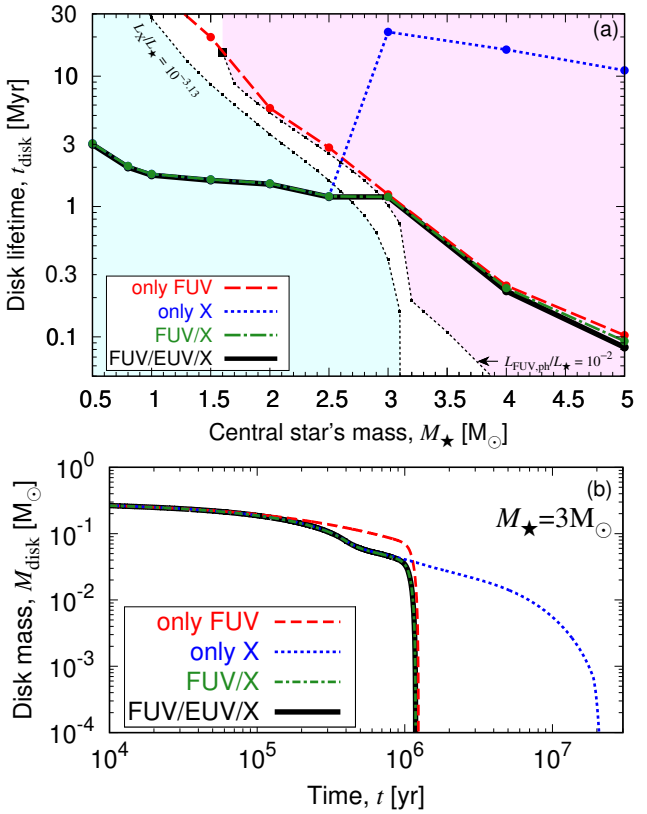

Figure 11. *Top panel.* Disk lifetime as a function of $M_\star$ in the cases with the FUV, EUV and X-ray PE (the black solid line), with only the FUV PE (red dashed), with only the X-ray PE (blue dotted) and with the FUV and X-ray PE (green dot-dashed). The two thin black dotted lines show the time when $Ro = {\rm Ro}_{\rm sat}$ (left; i.e., $L_{\rm X}/L_\star = 10^{-3.13}$) and $T_{\rm eff} = 7342\,{\rm K}$ (right; i.e., $L_{\rm FUV,ph}/L_\star = 10^{-2}$). The left shaded region (cyan) illustrates the phase in which the X-ray PE dominates, whereas the right (magenta) the FUV PE dominates. *Bottom panel.* Time evolution of disk mass, $M_{\rm disk}$, around a $3\,{\rm M}_\odot$ star.

Figure 11a also shows the time when stars reach $Ro = {\rm Ro}_{\rm sat}$ (i.e., $L_{\rm X} = 10^{-3.13}\,L_\star$; the maximum value of $L_{\rm X}$) and $T_{\rm eff} = 7342\,{\rm K}$ (i.e., $L_{\rm FUV,ph} = 10^{-2}\,L_\star$; as an indicative timescale for $\dot{M}_{\rm FUV}$ to increase). These timescales decrease with $M_\star$. This is because higher-mass stars have a shorter K-H timescale $\tau_{\rm KH}$ (see Eq. 1) and therefore develop a radiative core and have a hotter photosphere more rapidly. We note that $T_{\rm eff}$ of stars with less than $1.6\,{\rm M}_\odot$ never reaches 7342 K in the pre-MS and main-sequence (MS hereafter) phases, and therefore $L_{\rm FUV,ph}$ is always below $10^{-2}L_\star$.

In the cases with FUV, the disks around $\geq 2\,{\rm M}_\odot$ stars disperse after $L_{\rm FUV,ph}$ reaches $10^{-2}\,L_\star$. In the case with only the FUV PE, the disk lifetime around ~ 1.5–$3\,{\rm M}_\odot$ stars is almost the same as the timescale to reach $L_{\rm FUV,ph} = 10^{-2}\,L_\star$. Therefore, if the X-ray PE is less

effective, the disk lifetime around IM stars is determined by the stellar evolution. We note that even though $L_{\rm FUV}$ of 4 and 5 $M_\odot$ stars becomes luminous in the early phase, it takes time for $\dot{M}_{\rm acc}$ to decrease and for the disks to disperse. On the other hand, the disk lifetime around $\lesssim 1\,M_\odot$ stars in the case with only FUV exceeds 30 Myr. This is because $L_{\rm FUV}$ of low-mass stars is dominated by $L_{\rm FUV,acc}$, which is self-regulated; $L_{\rm FUV,acc}$ decreases along with decreasing $\dot{M}_{\rm acc}$ over time. Therefore the PE mainly by $L_{\rm FUV,acc}$ does not open a gap.

If we compare the cases with and without the X-ray PE, one finds that the disks around $\lesssim 2.5\,M_\odot$ stars disperse mainly by the X-ray PE. The influence of the EUV PE on $t_{\rm disk}$ is negligible in the entire mass range. Therefore, under the current settings, $\gtrsim 3\,M_\odot$ stars disperse mainly by the FUV PE, whereas $\lesssim 2.5\,M_\odot$ stars by the X-ray PE. We note that, however, although in this study we adopt the X-ray and EUV PE rates from the literature, they are still under debate (see Sect. 5.4). If our X-ray PE rate is overestimated, then the realistic $t_{\rm disk}$ should be in between $t_{\rm disk}$ of the fiducial case and that of "only FUV" case. Nevertheless, the importance of the $L_{\rm FUV,ph}$ evolution around IM stars is not affected by the uncertainty of the X-ray PE model.

In the high-mass side ($\gtrsim 3\,M_\odot$), $t_{\rm disk}$ decreases with $M_\star$ because of the shorter $\tau_{\rm KH}$ as described above. Here we explain why we obtain the same trend in the low-mass side. The $t_{\rm disk}$ value is almost the same as the timescale of the gap-opening, which occurs when $\dot{M}_{\rm acc}$ decreases down to $\dot{M}_{\rm PE}$ (see Sect. 4.1). Both have a similar dependence on $M_\star$. We chose the input parameter α to reproduce the observed relation $\dot{M}_{\rm acc} \propto M_\star^2$ (Sect. 3.4). Around low-mass stars, the X-ray PE dominates and therefore $\dot{M}_{\rm PE} \simeq \dot{M}_{\rm X}$. We adopt the X-ray PE model based on Owen et al. (2012) which is in proportion to $L_{\rm X}$. Since Fig. 5 shows that $L_{\rm X}$ is roughly proportional to $M_\star^{1.6}$ in the case of 1-Myr-old low-mass stars. Since both $\dot{M}_{\rm acc}$ and $\dot{M}_{\rm PE}$ have a similar correlation with $M_\star$, the gap-opening timescale is determined by the timescale for $\dot{M}_{\rm acc}$ to decrease, that is, the viscous timescale $\tau_{\rm vis}$ (Clarke et al. 2001). Given that $\nu_{\rm vis} \propto M_\star$ (see Sect. 3.4) and that we assume R_1 does not correlate with $M_\star$, $\tau_{\rm vis} \propto M_\star^{-1}$. Therefore $\dot{M}_{\rm acc}$ decreases faster with $M_\star$ and therefore $t_{\rm disk}$ decreases with $M_\star$. We note that for this correlation, Eq. 20 is essentially important because this gives the relation $\nu_{\rm vis} \propto M_\star$ (see discussions in **Sect. 5.3**).

5. DISCUSSION

5.1. *Comparison with observations*

In this subsection, we compare our results with observations. Here we focus only on the gas disk lifetime (see Sect. 1 for dust disk lifetimes): recent Hα observations have revealed that the gas disk lifetime around IM stars is shorter than low-mass stars (Kennedy & Kenyon 2009; Yasui et al. 2014). This is consistent with our results of $t_{\rm disk}$ in Fig. 11a. We again stress that the realistic $L_{\rm FUV,ph}$ model with stellar evolution is crucial for this trend in the high-mass side, whereas the $L_{\rm X}$ and α models are important in the low-mass side. Since we have not explored the dependence on the input parameters and the PE models are still under debate, we limit ourselves to focus only on the qualitative results in this study. We leave the quantitatively detailed discussions for future studies.

5.2. *Dependence on the variety in X-ray luminosity*

We have found that disks around $\lesssim 2.5\,M_\odot$ stars are dispersed mainly by the X-ray PE and therefore $t_{\rm disk}$ depends on $L_{\rm X}$. Observations have revealed that stellar $L_{\rm X}$ has a large variety. Although in this article we have adopted the empirical relation of Wright et al. (2011, see Eq. 9), the observed data of $R_{\rm X}$ (see, e.g., Preibisch et al. 2005) exhibit a variety by a factor of 4.5 (= 0.65 dex). Moreover, although we have assumed $P_{\rm rot} = 3$ days, the observed rotational period of pre-MS stars has a variety from ~ 1 to 10 days (see Sect. 2.5). In this section, we explore the influence of these varieties on the results of $t_{\rm disk}$.

Figures 12a and 12b show the $L_{\rm X}$ evolution of $3\,M_\odot$ and $1\,M_\odot$ stars, respectively. We consider the cases with $P_{\rm rot} = 1$ day and 10 days, and with $L_{\rm X}$ multiplied or divided by a factor of 4.5. We find that $1\,M_\odot$ stars develop a radiative core at $\simeq 10$ Myr and until then pre-MS stars are in the saturated regime irrespective of $P_{\rm rot}$, whereas it happens for $3\,M_\odot$ stars in the early ($\simeq 0.4$ Myr) phase. We note that Tu et al. (2015) claimed that $L_{\rm X}$ of $1\,M_\odot$ MS stars has a large variety depending on the $P_{\rm rot}$. This is because $\tau_{\rm conv}$ of $1\,M_\odot$ MS stars is short enough for their $L_{\rm X}$ to depend on $P_{\rm rot}$ (see also Eq. 9). However, our results show that $L_{\rm X}$ of pre-MS $1\,M_\odot$ stars does not depend on $P_{\rm rot}$ until $\simeq 10$ Myr.

Figure 12c shows $t_{\rm disk}$ with different $L_{\rm X}$ models. Here we adopt fiducial settings other than $L_{\rm X}$. We find that the variation in $P_{\rm rot}$ has little impact on $t_{\rm disk}$. On the other hand, if we change $L_{\rm X}$ by a factor of 4.5, $t_{\rm disk}$ changes by up to 1 dex. The variation of $L_{\rm X}$ has a larger impact on $t_{\rm disk}$ around lower-mass stars. Therefore for the detailed comparison with observed disk fractions with time, we need to consider the $L_{\rm X}$ variation as claimed by Kimura et al. (2016).

The trend of $t_{\rm disk}$ with $M_\star$ depends on different $L_{\rm X}$ models: $t_{\rm disk}$ decreases with increasing $M_\star$ in the low $L_{\rm X}$ case, whereas $t_{\rm disk}$ of $< 3\,M_\odot$ stars is almost con-

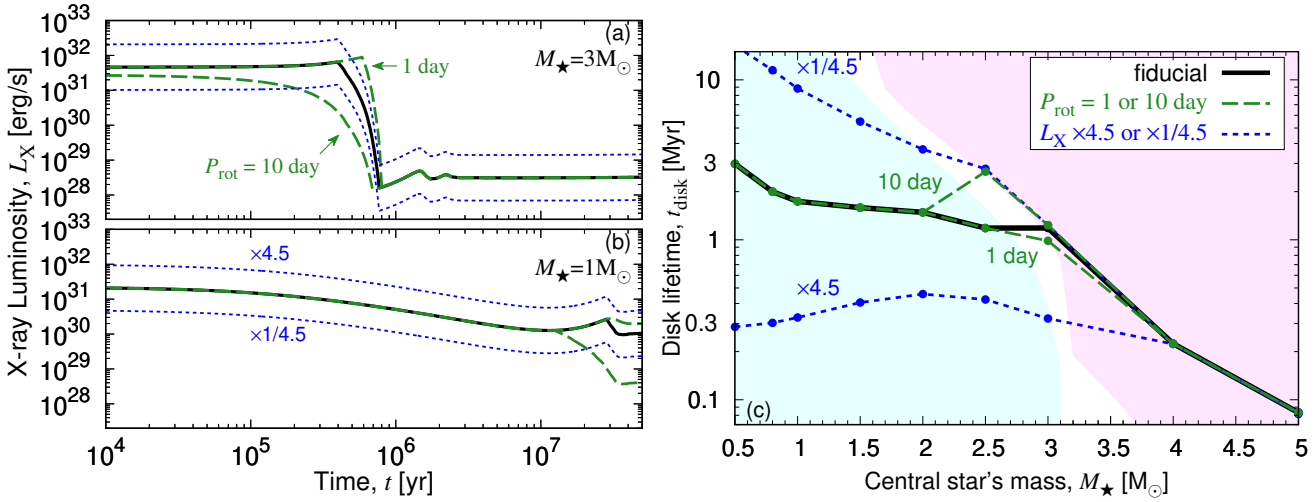

Figure 12. (Left panel) Temporal evolutions of L_X of a $3\,M_\odot$ (top panel) and $1\,M_\odot$ (bottom) star. The black solid lines show the fiducial one (i.e., $P_{rot} = 3$ days). The dashed green lines show the cases with $P_{rot} = 1$ day (top) and 10 days (bottom). The dotted blue lines are $L_X \times 4.5$ (top) and $L_X/4.5$ (bottom), highlighting the observed scatter. (Right) t_{disk} with the different L_X models. The cyan and magenta shades are the same as in Fig. 11a. We note that the cyan region depends on P_{rot} (see the left panel).

stant in the high L_X case. For the former, the reason is the same as the fiducial case (i.e., the shorter τ_{vis}; see Sect. 4.3). For the latter, $\dot{M}_X \gg \dot{M}_{acc}$ from the beginning and therefore the gap-opening timescale ($\sim t_{disk}$) is determined by $\tau_{PE}(R_{gap}) = \Sigma/\dot{\Sigma}_{PE}$, where R_{gap} is the radius where the PE opens a gap. Below, we briefly show that $\tau_{PE}(R_{gap})$ is insensitive to $M_\star$. First, $R_{gap} \propto M_\star$ because the location of the peak of $\dot{\Sigma}_X$ is proportional to $M_\star$ (see Sect. 3.2). Since we assume $\Sigma \propto R^{-1}M_\star$ as an initial condition, the initial Σ at R_{gap} does not depend on $M_\star$. Secondly, $\dot{\Sigma}_{PE}(R_{gap}) \simeq \dot{\Sigma}_X \propto L_X R_{gap}^{-2}$ (see Eq. 15), where $L_X \propto M_\star^{1.6}$ but $R_{gap}^{-2} \propto M_\star^{-2}$. These two opposite effects make the peak $\dot{\Sigma}_X$ value almost constant with $M_\star$. Therefore, τ_{PE} (thus t_{disk}) of $< 3\,M_\star$ stars is insensitive to $M_\star$ in the high L_X case .

5.3. Dependence on the variety in viscosity

We have adopted $\alpha \propto M_\star$ to reproduce the observed relation ($\dot{M}_{acc} \propto M_\star^2$; see Sect. 3.4), but the physical origin of this relation is still unclear. **In addition, the absolute value of α is also under debate. As a fiducial value,** we adopt a relatively large α value ($= 10^{-2}\,(M_\star/M_\odot)$) assuming that disks are turbulent. However, recent observations (e.g., Pinte et al. 2016; Flaherty et al. 2017) and theoretical studies (see, e.g., Turner et al. 2014, and references therein) have suggested a low α (e.g., $\lesssim 10^{-3}$ from the observations).

To explore the dependence of t_{disk} on the α model, we simulate disk evolutions with $\alpha = 10^{-2}$ (i.e., constant α with $M_\star$) and $\alpha = 10^{-3}\,(M_\star/M_\odot)$ (i.e., 10 times lower than the fiducial model).

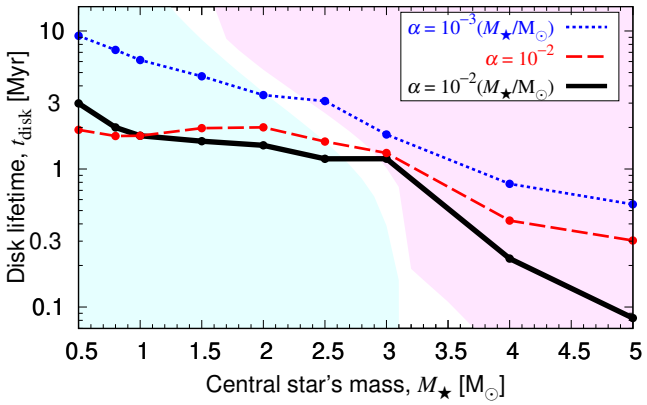

Figure 13. Disk lifetime, t_{disk}, with different α models: $\alpha = 10^{-2}(M_\star/M_\odot)$ (black solid; fiducial), $\alpha = 10^{-2}$ (red dashed), and $\alpha = 10^{-3}(M_\star/M_\odot)$ (blue dotted). The cyan and magenta shades are the same as in Fig. 11a.

Figure 13 shows that the decreasing t_{disk} with α in the high-mass side ($\geq 3\,M_\odot$) remains even if we adopt a different alpha model, because the rapid increase of $L_{FUV,ph}$ has a dominant role.

We note that the variety in α affects the t_{disk} values: A lower α by a factor of 10 results in a larger t_{disk} by a factor of $\simeq 3$ (as shown in figure 11 of Gorti et al. 2009). We also note that if α is constant with $M_\star$, the t_{disk} value is also constant with $M_\star$ ($\simeq 2$ Myr) in the range $M_\star \leq 3\,M_\odot$. Therefore, **to compare theoretical t_{disk} values with observations,** it is crucial to understand the origin of the rela-

tion $\dot{M}_{\rm acc} \propto M_\star^2$ **and constrain the absolute value of α in protoplanetary disks**.

5.4. *Model caveats*

In this subsection we describe the caveats on the PE models, evolution of dust disks, magnetohydrodynamic (MHD) winds, and the variations of input parameters.

We point out two issues on the PE models. First, although we adopt the X-ray PE model by Owen et al. (2012), their $\dot{M}_{\rm X}$ is higher than that of recent RHD simulations with a self-consistent thermochemistry by Wang & Goodman (2017); Nakatani et al. (2018a). Therefore, although our results suggest that the disks around $\lesssim 2.5\,{\rm M}_\odot$ stars disperse mainly by the X-ray PE (Sect. 4.1), $t_{\rm disk}$ of $\lesssim 2.5\,{\rm M}_\odot$ stars may be underestimated. Future works should investigate the long-term disk evolution with the updated X-ray PE rate. **Secondly,** the PE may be suppressed in particular in the early phase in the outer region due to the absorption of high-energy photons. These photons can be shielded by dense gas such as accretion flows onto the star (Alexander et al. 2004), inner disk winds (Bai 2017; Takasao et al. 2018), stellar winds (Hollenbach et al. 2000) and dust grains in the disk atmosphere (Nakatani et al. 2018b). If the high-energy photons are shielded, the PE rate can decrease by orders of magnitude and the PE profiles can also be changed (see also Sect. 4.2).

There are two issues on the luminosity and spectra of stellar high-energy photons. First, in this article we have used a simple model of $\Phi_{\rm EUV}$, but this is quite uncertain (Sect. 2.4). Bouret & Catala (1998) suggested Herbig Ae/Be stars have $\Phi_{\rm EUV} \sim 10^{43}$–$10^{45}$ using an indirect estimation. Although the EUV PE has a marginal effect on the disk evolution in our results, we expect that future works constrain $\Phi_{\rm EUV}$ of IM stars more precisely. Secondly, the hardness of the X-ray spectra of young stars remains a matter of debate. Some observations have suggested that the X-ray spectra of accreting stars may be softer (e.g., Kastner et al. 2002, 2004). Since Gorti et al. (2009) have shown that a softer X-ray spectrum results in the larger PE rate even with the same $L_{\rm X}$ (see their figure 9). Future studies should investigate the influence of the evolution of the X-ray hardness on the disk evolution.

The uncertainties and varieties in the PE models above would be important for some observational results. Although most IM stars have a shorter inner disk lifetime (see Sect. 5.1), some have a long disk lifetime **(e.g., Panić et al. 2008; Fedele et al. 2017; Booth et al. 2019; Miley et al. 2019; Muro-Arena et al. 2020)**. These long-lived disks may have a lower PE rate. Since most of these long-lived disks around Herbig stars are well studied due to the relative ease of detecting their large bright disks, there is a lot of existing high quality data for theoretical models to be compared with. Theoretical models should be compared in detail with and explain these observations in future.

We stress the importance of the dust disk evolution which is not considered in this paper. Previous studies have found that gas and dust disk lifetimes can differ (see, e.g., Takeuchi et al. 2005; Alexander & Armitage 2007; Gorti et al. 2015; Owen & Kollmeier 2019). Since IR observations trace the small dust grains, we need to simulate the long-term evolution of gas and dust to compare theoretical models with IR observations. The amount of dust grains in the disk atmosphere may also affect the FUV PE rate (Gorti et al. 2015; Nakatani et al. 2020). However, the motion and evolution of dust grains are quite complicated: we need to consider a number of effects such as radial drift (Adachi et al. 1976), gas pressure gradient (Taki et al. 2016, 2020), fragmentation and collisional cascade (Kobayashi & Tanaka 2010), the entrainment in the PE or MHD disk winds (Gorti et al. 2015; Miyake et al. 2016; Bai 2016; Franz et al. 2020). Future studies with the dust evolution and stellar evolution around IM stars are needed to investigate the realistic lifetimes of dust disks.

In this paper we have not included MHD disk winds, **but recently much attention has been paid to them (e.g., Suzuki & Inutsuka 2009; Fromang et al. 2013; Lesur et al. 2013; Bai & Stone 2013a; Bai 2017; Wang et al. 2019).** The MHD winds carry away not only mass but also angular momentum (so-called wind-driven accretion; Bai & Stone 2013b; Bai 2016; Suzuki et al. 2016). Kunitomo et al. (2020) claimed that the MHD and PE winds have different roles (see also recent radiation-MHD simulations by Wang et al. 2019; Rodenkirch et al. 2020; Gressel et al. 2020) and both winds and the wind-driven accretion should be considered for a realistic disk evolution, in particular for disks with weak turbulence. We will investigate the long-term disk evolution around IM stars including both winds in our next paper.

We have not varied input parameters in this paper. **The variety of the initial disk condition, $M_{\rm d,ini}$ and R_1, should be related** to the properties of parental clouds using a disk formation model (Takahashi et al. 2013; Kimura et al. 2016). For a detailed compar-

ison with the observations of disk fractions over time, we need Monte Carlo simulations covering the variety of input parameters ($M_{\rm d,ini}$ R_1**, and also** α**;** **Alexander & Armitage 2009**; **Kimura et al. 2016**).

Finally, we discuss the variety in stellar evolution. Although in this paper we adopted the birthline based on the standard star formation scenario, recent studies have shown that the luminosity of the birthline depend on star formation processes (such as the variety in the entropy of accreting materials or deuterium abundance; see Baraffe et al. 2009; Hosokawa et al. 2011; Tognelli et al. 2015; Kunitomo et al. 2017; Kuffmeier et al. 2018). Stellar $T_{\rm eff}$ depends on the metallicity and the mixing-length parameter $\alpha_{\rm MLT}$: a lower metallicity or larger $\alpha_{\rm MLT}$ results in the higher $T_{\rm eff}$ (Kippenhahn & Weigert 1990). Although in this paper we have adopted the solar metallicity and $\alpha_{\rm MLT} = 2.0$[7], the varieties of these parameters affect the $T_{\rm eff}$ evolution and therefore the $L_{\rm FUV,ph}$ and $\Phi_{\rm EUV,ph}$ evolutions.

5.5. Implications for planet formation

The disk evolution models have important implications for plant formation. **Since planets form and evolve in a protoplanetary disk, their characteristics may reflect the disk properties. For example, the** orbital configuration of planets around IM stars is different from low-mass stars**: there is a paucity of close-in planets around $\gtrsim 2\,{\rm M}_\odot$ stars (e.g., Sato et al. 2008). One possible origin is the different disk evolution: the rapid disk dispersal may hinder planets from migrating inward (e.g., Burkert & Ida 2007; Currie 2009; Kunitomo et al. 2011).** Radial velocity surveys have revealed the occurrence rate of detected giant planets depends upon $M_\star$ (e.g., Johnson et al. 2010; Reffert et al. 2015). The amount and/or composition of planet atmospheres can give an indication as to when or where the planet was formed in a disk (Guillot & Hueso 2006; Ogihara et al. 2020; Miley et al. 2021). We expect that our disk evolution models also lead to the understanding of planet formation processes around IM stars.

6. SUMMARY AND CONCLUSIONS

We investigated the long-term disk evolution around 0.5–5 $\rm M_\odot$ stars considering the viscous accretion, the PE mass loss by stellar FUV, EUV and X-rays, and stellar evolution. We started calculations from the early phase and initial conditions with a compact ($R_1 = 50\,$au) and massive ($M_{\rm d,ini} = 0.1\,M_\star$) disk.

We found that *the nature of the emission of stellar high-energy photons changes with time*: low-mass stars strongly emit X-rays until the typical disk lifetime (i.e., several Myr), whereas the X-ray luminosity of higher-mass stars decreases and instead their FUV luminosity rapidly increases due to stellar evolution (e.g., at around 1 Myr in the case of $3\,{\rm M}_\odot$ stars). The critical mass is $\sim 2.5\,{\rm M}_\odot$ because the K-H timescale becomes comparable to the disk dispersal timescale. Therefore the effect of stellar evolution is not negligible as assumed in previous works and should be considered for realistic disk evolution models around IM stars.

Our results show that if we consider all the PE mechanisms (X-ray, EUV and FUV) with stellar evolution, then $t_{\rm disk}$ *decreases with* $M_\star$. Hα observations have also suggested the same trend. For the detailed comparison with observations, our models should be refined in future work. Although we have adopted the PE models from the literature, they have recently been revisited with a self-consistent thermochemistry. Our models simulate the evolution of gas disks, but the evolution of dust disks is crucially important for the comparison with IR observations. We considered viscous accretion and photoevaporation, but other physical processes such as MHD disk winds or magnetic braking should also be considered simultaneously. We have not surveyed large parameter ranges of R_1, $M_{\rm d,ini}$, and α.

The evolution models of protoplanetary disks are crucially important for planet formation theory. We expect that the disk evolution models presented in this paper lead to the understanding of planet formation around IM stars.

[7] Although Kunitomo et al. (2011) described that $\alpha_{\rm MLT} = 1.5$, this was a typo. In standard solar models (see, e.g., Serenelli et al. 2009), $\alpha_{\rm MLT} \simeq 2.0$ is suggested.

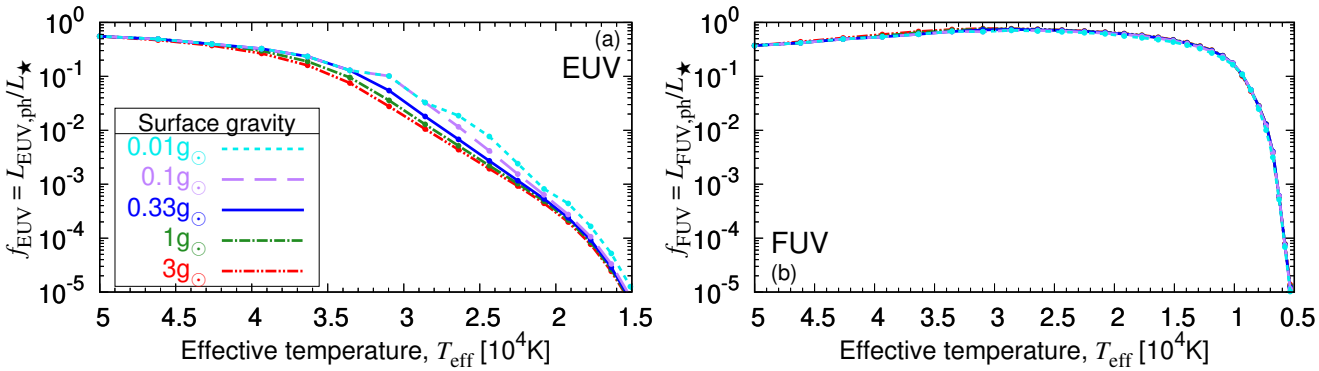

Figure 14. $f_{\rm EUV}$ (left panel) and $f_{\rm FUV}$ (right) with varying $g = 3\,{\rm g}_\odot$ (the red double dot-dashed lines), $1\,{\rm g}_\odot$ (green dot-dashed), $0.33\,{\rm g}_\odot$ (fiducial; blue solid), $0.1\,{\rm g}_\odot$ (purple dashed) and $0.01\,{\rm g}_\odot$ (cyan dotted).

ACKNOWLEDGMENTS

We are grateful for the simulation results of star formation provided by Dr. Steven W. Stahler. We are also grateful to Drs. Kei E. I. Tanaka, Chikako Yasui, Masahiro Ikoma, Taishi Nakamoto, Hideko Nomura, Philip J. Armitage, Richard D. Alexander, Jaehan Bae, Kenji Hamaguchi, Shinsuke Takasao, Shu-ichiro Inutsuka and Hiroshi Kobayashi for fruitful discussions and comments. We appreciate the constructive comments of the anonymous referee, which helped us to improve this paper. M.K. and S.I. thank the University of Leeds for the financial support through the International Mobility Fund, and hospitality during their stay in Leeds. This work was supported by JSPS KAKENHI Grant Numbers 12J09296, 23244027, 15H02065, 16H02160, 17H01105, 17H01153 and 20K14542. The work of O.P. is funded by the Royal Society Dorothy Hodgkin Fellowship. J.M.M. is supported through the University of Leeds Doctoral Scholarship.

Software: MESA (version 2258, Paxton et al. 2011), Cloudy (version 13.04, Ferland et al. 2013), Numpy (van der Walt et al. 2011), WebPlotDigitizer (version 4.2; https://automeris.io/WebPlotDigitizer)

APPENDIX

A. DEPENDENCE OF PHOTOSPHERIC UV LUMINOSITY ON THE STELLAR SURFACE GRAVITY

In Sect. 2.2, we derived the empirical formulae of photospheric FUV and EUV luminosities in the case of $g = 0.33\,{\rm g}_\odot$. We note that there is a variety in $\log g$ of 0.5–5 $M_\odot$ pre-MS stars; from 0.1 to 10 Myr, it ranges from 2.7 to 4.3. Figure 14 shows the weak dependence of $f_{\rm EUV}$ and $f_{\rm FUV}$ on $\log g$. We find that the difference of $f_{\rm FUV}$ from the fiducial case with $0.33\,{\rm g}_\odot$ is at most 13%, but that of $f_{\rm EUV}$ is up to a factor of three. In this paper we neglect this weak dependence for simplicity.

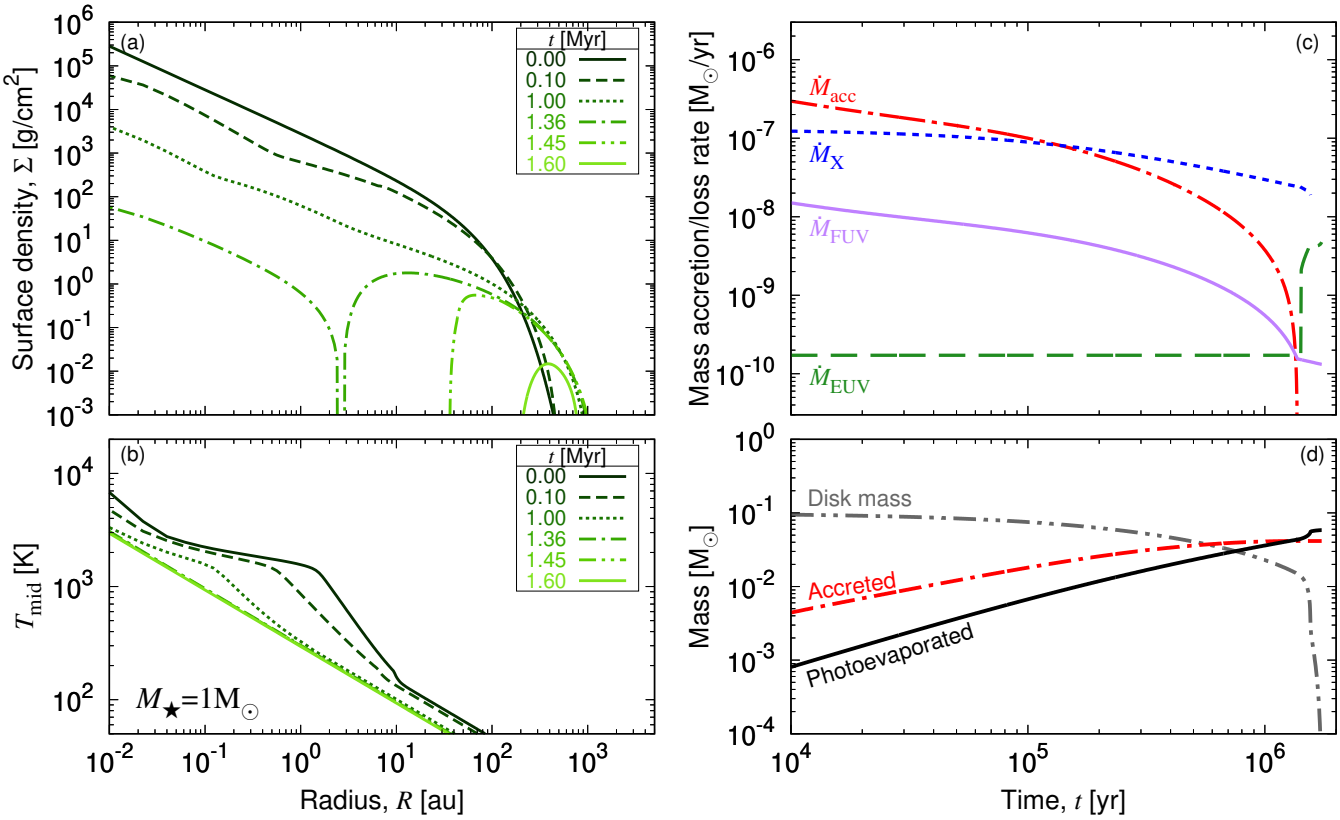

Figure 15. Same as Fig. 8 but around a $1\,M_\odot$ star.

B. DISK EVOLUTION AROUND LOW-MASS STARS

In this Appendix, we show the disk evolution around low-mass stars in our model. Since the X-ray PE is a matter of debate (see Sect. 5.4), it should be noted that the results may be updated in future work.

Figure 15 shows the disk evolution around a $1\,M_\odot$ star. The qualitative behavior of the surface density evolution is the same as the $3\,M_\odot$ star case (Sect. 4.1). However, unlike the case of IM stars (Fig. 8), $\dot{M}_{\rm X}$ is always larger than $\dot{M}_{\rm EUV}$ and $\dot{M}_{\rm FUV}$ (see however the caveats in Sect. 5.4). This is because the $L_{\rm X}$ of $\lesssim 1\,M_\odot$ young stars is in the saturated regime and therefore as large as $\sim 10^{29}$–10^{31} erg/s. Therefore most materials are lost by either accretion or the X-ray PE.

We note that, as described in Kunitomo et al. (2020, see their section 4.4), we see the gradual decrease of $\dot{M}_{\rm X}$ over 3 Myr, but the qualitative behavior described above is the same as the cases with the constant $L_{\rm X}$ cases in the previous works (e.g., Owen et al. 2010). This is expected from the long K-H timescale of low-mass stars (see Sect. 1).

REFERENCES

Adachi, I., Hayashi, C., & Nakazawa, K. 1976, Progress of Theoretical Physics, 56, 1756, doi: 10.1143/PTP.56.1756

Adams, F. C., Hollenbach, D., Laughlin, G., & Gorti, U. 2004, ApJ, 611, 360, doi: 10.1086/421989

Alexander, R., Pascucci, I., Andrews, S., Armitage, P., & Cieza, L. 2014, in Protostars and Planets VI, ed. H. Beuther, R. S. Klessen, C. P. Dullemond, & T. Henning (University of Arizona Press), 475–496, doi: 10.2458/azu_uapress_9780816531240-ch021

Alexander, R. D., & Armitage, P. J. 2007, MNRAS, 375, 500, doi: 10.1111/j.1365-2966.2006.11341.x

—. 2009, ApJ, 704, 989, doi: 10.1088/0004-637X/704/2/989

Alexander, R. D., Clarke, C. J., & Pringle, J. E. 2004, MNRAS, 348, 879, doi: 10.1111/j.1365-2966.2004.07401.x

—. 2006a, MNRAS, 369, 229, doi: 10.1111/j.1365-2966.2006.10294.x

—. 2006b, MNRAS, 369, 216, doi: 10.1111/j.1365-2966.2006.10293.x

Andrews, S. M., Rosenfeld, K. A., Kraus, A. L., & Wilner, D. J. 2013, ApJ, 771, 129, doi: 10.1088/0004-637X/771/2/129
Andrews, S. M., Terrell, M., Tripathi, A., et al. 2018, ApJ, 865, 157, doi: 10.3847/1538-4357/aadd9f
Andrews, S. M., Wilner, D. J., Hughes, A. M., Qi, C., & Dullemond, C. P. 2010, ApJ, 723, 1241, doi: 10.1088/0004-637X/723/2/1241
Ansdell, M., Williams, J. P., Trapman, L., et al. 2018, ApJ, 859, 21, doi: 10.3847/1538-4357/aab890
Armitage, P. J. 2000, A&A, 362, 968. https://arxiv.org/abs/astro-ph/0007044
Bahcall, J. N., Basu, S., Pinsonneault, M., & Serenelli, A. M. 2005, ApJ, 618, 1049, doi: 10.1086/426070
Bai, X.-N. 2016, ApJ, 821, 80, doi: 10.3847/0004-637X/821/2/80
—. 2017, ApJ, 845, 75, doi: 10.3847/1538-4357/aa7dda
Bai, X.-N., & Stone, J. M. 2013a, ApJ, 767, 30, doi: 10.1088/0004-637X/767/1/30
—. 2013b, ApJ, 769, 76, doi: 10.1088/0004-637X/769/1/76
Balbus, S. A., & Hawley, J. F. 1991, ApJ, 376, 214, doi: 10.1086/170270
Baraffe, I., Chabrier, G., & Gallardo, J. 2009, ApJL, 702, L27, doi: 10.1088/0004-637X/702/1/L27
Booth, A. S., Walsh, C., Ilee, J. D., et al. 2019, ApJL, 882, L31, doi: 10.3847/2041-8213/ab3645
Bouret, J.-C., & Catala, C. 1998, A&A, 340, 163
Bouvier, J. 2008, A&A, 489, L53, doi: 10.1051/0004-6361:200810574
Burkert, A., & Ida, S. 2007, ApJ, 660, 845, doi: 10.1086/512538
Calvet, N., & Gullbring, E. 1998, ApJ, 509, 802, doi: 10.1086/306527
Calvet, N., Muzerolle, J., Briceño, C., et al. 2004, AJ, 128, 1294, doi: 10.1086/422733
Carpenter, J. M., Mamajek, E. E., Hillenbrand, L. A., & Meyer, M. R. 2006, ApJL, 651, L49, doi: 10.1086/509121
Castelli, F., & Kurucz, R. L. 2003, in IAU Symposium, Vol. 210, Modelling of Stellar Atmospheres, ed. N. Piskunov, W. W. Weiss, & D. F. Gray, A20. https://arxiv.org/abs/astro-ph/0405087
Chandrasekhar, S. 1961, Hydrodynamic and hydromagnetic stability
Clarke, C. J., Gendrin, A., & Sotomayor, M. 2001, MNRAS, 328, 485, doi: 10.1046/j.1365-8711.2001.04891.x
Cox, J., & Giuli, R. 1968, Gordon and Breach, New York, 401
Currie, T. 2009, ApJL, 694, L171, doi: 10.1088/0004-637X/694/2/L171
Ercolano, B., Drake, J. J., Raymond, J. C., & Clarke, C. C. 2008, ApJ, 688, 398, doi: 10.1086/590490
Ercolano, B., & Pascucci, I. 2017, Royal Society Open Science, 4, 170114, doi: 10.1098/rsos.170114
Fedele, D., Carney, M., Hogerheijde, M. R., et al. 2017, A&A, 600, A72, doi: 10.1051/0004-6361/201629860
Ferland, G. J., Porter, R. L., van Hoof, P. A. M., et al. 2013, RMxAA, 49, 137. https://arxiv.org/abs/1302.4485
Flaccomio, E., Damiani, F., Micela, G., et al. 2003, ApJ, 582, 398, doi: 10.1086/344536
Flaherty, K. M., Hughes, A. M., Rose, S. C., et al. 2017, ApJ, 843, 150, doi: 10.3847/1538-4357/aa79f9
Font, A. S., McCarthy, I. G., Johnstone, D., & Ballantyne, D. R. 2004, ApJ, 607, 890, doi: 10.1086/383518
Franz, R., Picogna, G., Ercolano, B., & Birnstiel, T. 2020, A&A, 635, A53, doi: 10.1051/0004-6361/201936615
Fromang, S., Latter, H., Lesur, G., & Ogilvie, G. I. 2013, A&A, 552, A71, doi: 10.1051/0004-6361/201220016
Gallet, F., & Bouvier, J. 2013, A&A, 556, A36, doi: 10.1051/0004-6361/201321302
Gorti, U., Dullemond, C. P., & Hollenbach, D. 2009, ApJ, 705, 1237, doi: 10.1088/0004-637X/705/2/1237
Gorti, U., & Hollenbach, D. 2009, ApJ, 690, 1539, doi: 10.1088/0004-637X/690/2/1539
Gorti, U., Hollenbach, D., & Dullemond, C. P. 2015, ApJ, 804, 29, doi: 10.1088/0004-637X/804/1/29
Gorti, U., Liseau, R., Sándor, Z., & Clarke, C. 2016, SSRv, 205, 125, doi: 10.1007/s11214-015-0228-x
Gregory, S. G., Adams, F. C., & Davies, C. L. 2016, MNRAS, 457, 3836, doi: 10.1093/mnras/stw259
Gressel, O., Ramsey, J. P., Brinch, C., et al. 2020, ApJ, 896, 126, doi: 10.3847/1538-4357/ab91b7
Güdel, M. 2004, A&A Rv, 12, 71, doi: 10.1007/s00159-004-0023-2
Guillot, T., & Hueso, R. 2006, Monthly Notices of the Royal Astronomical Society: Letters, 367, L47, doi: 10.1111/j.1745-3933.2006.00137.x
Hamaguchi, K., Yamauchi, S., & Koyama, K. 2005, ApJ, 618, 360, doi: 10.1086/423192
Hamidouche, M., Wang, S., & Looney, L. W. 2008, AJ, 135, 1474, doi: 10.1088/0004-6256/135/4/1474
Haworth, T. J., & Clarke, C. J. 2019, MNRAS, 485, 3895, doi: 10.1093/mnras/stz706
Hayashi, C. 1961, PASJ, 13, 450
Herbig, G. H. 1960, ApJS, 4, 337, doi: 10.1086/190050
Hernández, J., Calvet, N., Hartmann, L., et al. 2005, AJ, 129, 856, doi: 10.1086/426918
Hillenbrand, L. A., Strom, S. E., Vrba, F. J., & Keene, J. 1992, ApJ, 397, 613, doi: 10.1086/171819

Hollenbach, D., Johnstone, D., Lizano, S., & Shu, F. 1994, ApJ, 428, 654, doi: 10.1086/174276
Hollenbach, D. J., Yorke, H. W., & Johnstone, D. 2000, Protostars and Planets IV, 401
Hosokawa, T., Offner, S. S. R., & Krumholz, M. R. 2011, ApJ, 738, 140, doi: 10.1088/0004-637X/738/2/140
Huenemoerder, D. P., Schulz, N. S., Testa, P., Kesich, A., & Canizares, C. R. 2009, ApJ, 707, 942, doi: 10.1088/0004-637X/707/2/942
Ingleby, L., Calvet, N., Hernández, J., et al. 2011, AJ, 141, 127, doi: 10.1088/0004-6256/141/4/127
Johnson, J. A., Aller, K. M., Howard, A. W., & Crepp, J. R. 2010, PASP, 122, 905, doi: 10.1086/655775
Judge, P. G., Solomon, S. C., & Ayres, T. R. 2003, ApJ, 593, 534, doi: 10.1086/376405
Kastner, J. H., Huenemoerder, D. P., Schulz, N. S., Canizares, C. R., & Weintraub, D. A. 2002, ApJ, 567, 434, doi: 10.1086/338419
Kastner, J. H., Richmond, M., Grosso, N., et al. 2004, Nature, 430, 429, doi: 10.1038/nature02747
Kennedy, G. M., & Kenyon, S. J. 2009, ApJ, 695, 1210, doi: 10.1088/0004-637X/695/2/1210
Kimura, S. S., Kunitomo, M., & Takahashi, S. Z. 2016, MNRAS, 461, 2257, doi: 10.1093/mnras/stw1531
Kippenhahn, R., & Weigert, A. 1990, Stellar Structure and Evolution (Springer-Verlag)
Kobayashi, H., & Tanaka, H. 2010, Icarus, 206, 735, doi: 10.1016/j.icarus.2009.10.004
Komaki, A., Nakatani, R., & Yoshida, N. 2020, arXiv e-prints, arXiv:2012.14852. https://arxiv.org/abs/2012.14852
Kuffmeier, M., Frimann, S., Jensen, S. S., & Haugbølle, T. 2018, MNRAS, 475, 2642, doi: 10.1093/mnras/sty024
Kunitomo, M., Guillot, T., Takeuchi, T., & Ida, S. 2017, A&A, 599, A49, doi: 10.1051/0004-6361/201628260
Kunitomo, M., Ikoma, M., Sato, B., Katsuta, Y., & Ida, S. 2011, ApJ, 737, 66, doi: 10.1088/0004-637X/737/2/66
Kunitomo, M., Suzuki, T. K., & Inutsuka, S.-i. 2020, MNRAS, 492, 3849, doi: 10.1093/mnras/staa087
Lesur, G., Ferreira, J., & Ogilvie, G. I. 2013, A&A, 550, A61, doi: 10.1051/0004-6361/201220395
Liffman, K. 2003, PASA, 20, 337, doi: 10.1071/AS03019
Long, F., Herczeg, G. J., Harsono, D., et al. 2019, ApJ, 882, 49, doi: 10.3847/1538-4357/ab2d2d
Lynden-Bell, D., & Pringle, J. E. 1974, MNRAS, 168, 603
Mangeney, A., & Praderie, F. 1984, A&A, 130, 143
Miley, J. M., Panić, O., Booth, R. A., et al. 2021, MNRAS, 500, 4658, doi: 10.1093/mnras/staa3517
Miley, J. M., Panić, O., Haworth, T. J., et al. 2019, MNRAS, 485, 739, doi: 10.1093/mnras/stz426
Miyake, T., Suzuki, T. K., & Inutsuka, S.-i. 2016, ApJ, 821, 3, doi: 10.3847/0004-637X/821/1/3
Mohanty, S., Greaves, J., Mortlock, D., et al. 2013, ApJ, 773, 168, doi: 10.1088/0004-637X/773/2/168
Muro-Arena, G. A., Benisty, M., Ginski, C., et al. 2020, A&A, 635, A121, doi: 10.1051/0004-6361/201936509
Muzerolle, J., Luhman, K. L., Briceño, C., Hartmann, L., & Calvet, N. 2005, ApJ, 625, 906, doi: 10.1086/429483
Nakatani, R., Hosokawa, T., Yoshida, N., Nomura, H., & Kuiper, R. 2018a, ApJ, 865, 75, doi: 10.3847/1538-4357/aad9fd
—. 2018b, ApJ, 857, 57, doi: 10.3847/1538-4357/aab70b
Nakatani, R., Kobayashi, H., Kuiper, R., Nomura, H., & Aikawa, Y. 2020, arXiv e-prints, arXiv:2009.06438. https://arxiv.org/abs/2009.06438
Noyes, R. W., Hartmann, L. W., Baliunas, S. L., Duncan, D. K., & Vaughan, A. H. 1984, ApJ, 279, 763, doi: 10.1086/161945
Ogihara, M., Kunitomo, M., & Hori, Y. 2020, ApJ, 899, 91, doi: 10.3847/1538-4357/aba75e
Owen, J. E., Clarke, C. J., & Ercolano, B. 2012, MNRAS, 422, 1880, doi: 10.1111/j.1365-2966.2011.20337.x
Owen, J. E., Ercolano, B., Clarke, C. J., & Alexander, R. D. 2010, MNRAS, 401, 1415, doi: 10.1111/j.1365-2966.2009.15771.x
Owen, J. E., & Kollmeier, J. A. 2019, MNRAS, 487, 3702, doi: 10.1093/mnras/stz1591
Panić, O., Hogerheijde, M. R., Wilner, D., & Qi, C. 2008, A&A, 491, 219, doi: 10.1051/0004-6361:20079261
Parravano, A., Hollenbach, D. J., & McKee, C. F. 2003, ApJ, 584, 797, doi: 10.1086/345807
Pascucci, I., Testi, L., Herczeg, G. J., et al. 2016, ApJ, 831, 125, doi: 10.3847/0004-637X/831/2/125
Paxton, B., Bildsten, L., Dotter, A., et al. 2011, ApJS, 192, 3, doi: 10.1088/0067-0049/192/1/3
Picogna, G., Ercolano, B., Owen, J. E., & Weber, M. L. 2019, MNRAS, 487, 691, doi: 10.1093/mnras/stz1166
Pinte, C., Dent, W. R. F., Ménard, F., et al. 2016, ApJ, 816, 25, doi: 10.3847/0004-637X/816/1/25
Preibisch, T., Kim, Y.-C., Favata, F., et al. 2005, ApJS, 160, 401, doi: 10.1086/432891
Rasio, F. A., Tout, C. A., Lubow, S. H., & Livio, M. 1996, ApJ, 470, 1187, doi: 10.1086/177941
Rebull, L. M., Wolff, S. C., & Strom, S. E. 2004, AJ, 127, 1029, doi: 10.1086/380931
Reffert, S., Bergmann, C., Quirrenbach, A., Trifonov, T., & Künstler, A. 2015, A&A, 574, A116, doi: 10.1051/0004-6361/201322360
Ribas, Á., Bouy, H., & Merín, B. 2015, A&A, 576, A52, doi: 10.1051/0004-6361/201424846

Rodenkirch, P. J., Klahr, H., Fendt, C., & Dullemond, C. P. 2020, A&A, 633, A21, doi: 10.1051/0004-6361/201834945

Sato, B., Izumiura, H., Toyota, E., et al. 2008, PASJ, 60, 539, doi: 10.1093/pasj/60.3.539

Serenelli, A. M., Basu, S., Ferguson, J. W., & Asplund, M. 2009, ApJL, 705, L123, doi: 10.1088/0004-637X/705/2/L123

Shakura, N. I., & Sunyaev, R. A. 1973, A&A, 24, 337

Siess, L., Dufour, E., & Forestini, M. 2000, A&A, 358, 593

Stahler, S. W. 1988, ApJ, 332, 804, doi: 10.1086/166694

Stahler, S. W., & Palla, F. 2005, The Formation of Stars

Stelzer, B., Robrade, J., Schmitt, J. H. M. M., & Bouvier, J. 2009, A&A, 493, 1109, doi: 10.1051/0004-6361:200810540

Suzuki, T. K., Imada, S., Kataoka, R., et al. 2013, PASJ, 65, 98, doi: 10.1093/pasj/65.5.98

Suzuki, T. K., & Inutsuka, S.-i. 2009, ApJL, 691, L49, doi: 10.1088/0004-637X/691/1/L49

Suzuki, T. K., Ogihara, M., Morbidelli, A., Crida, A., & Guillot, T. 2016, A&A, 596, A74, doi: 10.1051/0004-6361/201628955

Takahashi, S. Z., Inutsuka, S.-i., & Machida, M. N. 2013, ApJ, 770, 71, doi: 10.1088/0004-637X/770/1/71

Takasao, S., Tomida, K., Iwasaki, K., & Suzuki, T. K. 2018, ApJ, 857, 4, doi: 10.3847/1538-4357/aab5b3

Takeuchi, T., Clarke, C. J., & Lin, D. N. C. 2005, ApJ, 627, 286, doi: 10.1086/430393

Taki, T., Fujimoto, M., & Ida, S. 2016, A&A, 591, A86, doi: 10.1051/0004-6361/201527732

Taki, T., Kuwabara, K., Kobayashi, H., & Suzuki, T. K. 2020, arXiv e-prints, arXiv:2004.08839. https://arxiv.org/abs/2004.08839

Tanaka, K. E. I., Nakamoto, T., & Omukai, K. 2013, ApJ, 773, 155, doi: 10.1088/0004-637X/773/2/155

Telleschi, A., Güdel, M., Briggs, K. R., Audard, M., & Palla, F. 2007, A&A, 468, 425, doi: 10.1051/0004-6361:20066565

Tognelli, E., Prada Moroni, P. G., & Degl'Innocenti, S. 2015, MNRAS, 454, 4037, doi: 10.1093/mnras/stv2254

Tu, L., Johnstone, C. P., Güdel, M., & Lammer, H. 2015, A&A, 577, L3, doi: 10.1051/0004-6361/201526146

Turner, N. J., Fromang, S., Gammie, C., et al. 2014, Protostars and Planets VI, 411, doi: 10.2458/azu_uapress_9780816531240-ch018

van den Ancker, M. E., The, P. S., Tjin A Djie, H. R. E., et al. 1997, A&A, 324, L33

van der Walt, S., Colbert, S. C., & Varoquaux, G. 2011, Computing in Science and Engineering, 13, 22, doi: 10.1109/MCSE.2011.37

Velikhov, E. 1959, Sov. Phys. JETP, 36, 995

Vilhu, O., & Rucinski, S. M. 1983, A&A, 127, 5

Villaver, E., & Livio, M. 2009, ApJL, 705, L81, doi: 10.1088/0004-637X/705/1/L81

Villebrun, F., Alecian, E., Hussain, G., et al. 2019, A&A, 622, A72, doi: 10.1051/0004-6361/201833545

Wang, L., Bai, X.-N., & Goodman, J. 2019, ApJ, 874, 90, doi: 10.3847/1538-4357/ab06fd

Wang, L., & Goodman, J. 2017, ApJ, 847, 11, doi: 10.3847/1538-4357/aa8726

Williams, J. P., & Cieza, L. A. 2011, ARA&A, 49, 67, doi: 10.1146/annurev-astro-081710-102548

Wright, N. J., Drake, J. J., Mamajek, E. E., & Henry, G. W. 2011, ApJ, 743, 48, doi: 10.1088/0004-637X/743/1/48

Yasui, C., Kobayashi, N., Tokunaga, A. T., & Saito, M. 2014, MNRAS, 442, 2543, doi: 10.1093/mnras/stu1013

Zahn, J.-P. 1977, A&A, 57, 383

Zinnecker, H., & Preibisch, T. 1994, A&A, 292, 152